Impact of Wave–Vortical Interactions on Oceanic Submesoscale Lateral Dispersion

GERARDO HERNÁNDEZ-DUEÑAS,[a] M.-PASCALE LELONG,[b] AND LESLIE M. SMITH[c,d]

[a] Instituto de Matemáticas, Universidad Nacional Autónoma de México–Campus Juriquilla, Querétaro, México
[b] NorthWest Research Associates, Redmond, Washington
[c] Department of Mathematics, University of Wisconsin–Madison, Madison, Wisconsin
[d] Department of Engineering Physics, University of Wisconsin–Madison, Madison, Wisconsin

(Manuscript received 8 December 2020, in final form 12 July 2021)

ABSTRACT: Submesoscale lateral transport of Lagrangian particles in pycnocline conditions is investigated by means of idealized numerical simulations with reduced-interaction models. Using a projection technique, the models are formulated in terms of wave-mode and vortical-mode nonlinear interactions, and they range in complexity from full Boussinesq to waves-only and vortical-modes-only (QG) models. We find that, on these scales, most of the dispersion is done by vortical motions, but waves cannot be discounted because they play an important, albeit indirect, role. In particular, we show that waves are instrumental in filling out the spectra of vortical-mode energy at smaller scales through nonresonant vortex–wave–wave triad interactions. We demonstrate that a richer spectrum of vortical modes in the presence of waves enhances the effective lateral diffusivity, relative to QG. Waves also transfer energy upscale to vertically sheared horizontal flows that are a key ingredient for internal-wave shear dispersion. In the waves-only model, the dispersion rate is an order of magnitude smaller and is attributed entirely to internal-wave shear dispersion.

KEYWORDS: Dispersion; Eddies; Internal waves; Nonlinear models

1. Introduction

Motivation for this study comes from several dye-tracer and Lagrangian float release experiments conducted in the pycnocline over the last three decades. Surprisingly, these observations, made in widely disparate ocean environments with varying degrees of mesoscale activity, consistently found $O(1)$ m^2 s^{-1} effective lateral diffusivities on scales from 100 m to 10 km. Experiments took place in open-ocean environments, for example, the North Atlantic Tracer Release Experiment (NATRE) experiment (Ledwell et al. 1993), in quiescent LatMix 2011 Sargasso Sea summertime conditions dominated by internal waves (Shcherbina et al. 2015; Lien and Sanford 2019; Sundermeyer et al. 2020b), and in continental shelf waters such as the Coastal Mixing and Optics (CMO) experiment (Sundermeyer and Ledwell 2001; Ledwell et al. 2004; Sundermeyer et al. 2005). Yet, despite a significant observational effort, the dynamics responsible for the effective lateral dispersion rate on these scales remain, by and large, not well understood.

Lateral dispersion in this regime, known as the submesoscale, governs pollutant dispersal and the spreading of plankton and fish colonies (Rypina et al. 2014), which strongly impact coastal communities and marine ecosystems. On a fundamental level, submesoscale lateral dispersion represents a pathway from larger-scale stirring toward three-dimensional mixing, important for understanding how energy is cascaded from the mesoscale toward dissipative isotropic scales (McWilliams 2008).

Submesoscale flow components in the stratified interior include internal waves and vortical modes. Idealized theoretical and numerical studies (Holmes-Cerfon et al. 2011; Bühler et al. 2013) have shown that dispersion by internal waves alone is too weak and cannot account for observed diffusivities. In their analysis of relative dispersion in the Antarctic Circumpolar Current, Balwada et al. (2021) find that superimposing near-inertial oscillations onto numerically simulated particle trajectories does not alter dispersion characteristics. These authors demonstrate that the presence of energetic near-inertial waves is incompatible with usage of commonly used dispersion metrics (e.g., finite-size Lyapunov exponents and second-order structure functions). Therefore, they conclude that waves can be safely filtered out in dispersion studies, as is routinely done in observations (Essink et al. 2019). Our study will show that, while internal waves may not contribute directly, they play a more subtle role than previously recognized in modifying submesoscale lateral dispersion.

Vortical modes account for linear potential vorticity (PV) of the flow (Müller et al. 1986). Examples of vortical-mode flows at the submesoscale include submesoscale coherent vortices and rotating stratified turbulence. Polzin and Ferrari (2004) analyzed NATRE data and attributed to vortical modes the submesoscale signal that could not be reconciled with linear internal waves. This led them to conclude that vortical modes were responsible for the observed $O(1)$ m^2 s^{-1} diffusivity on these scales. Numerical simulations by Sundermeyer and Lelong (2005) tested the idea first proposed by Sundermeyer (1998) that vortical modes in the ocean interior, created by geostrophic adjustment of well-mixed fluid patches following wave-breaking events, may account for $O(1)$ lateral diffusivities recorded during the CMO experiment (Sundermeyer and Ledwell 2001). These simulations reproduced qualitative characteristics of the dispersion observations, but could not attain the energy levels recorded at the CMO site.

Several studies have attempted to understand whether dispersion in the ocean is local, i.e., governed by comparable scales, or nonlocal and governed by larger scales (LaCasce 2008; Beron-Vera and LaCasce 2016). Local dynamics are

Corresponding author: Gerardo Hernández-Dueñas, hernandez@im.unam.mx

DOI: 10.1175/JPO-D-20-0299.1

associated with spectral kinetic energy slopes less than -3 and nonlocal dynamics with steeper spectra. The local/nonlocal dispersion interpretation was originally developed for two-dimensional turbulent flows (Kraichnan 1967) and later applied in the interpretation of quasi-2D geophysical flows, for example (Salmon 1983; Rhines 1988). In the ocean, interpretation of dispersion in terms of local/nonlocal statistics has proven difficult, in part due to the presence of near-inertial waves that can increase energy levels at small scales without having much of an impact on the relative dispersion of drifter pairs (Beron-Vera and LaCasce 2016; Essink et al. 2019; Balwada et al. 2021).

The majority of submesoscale dispersion studies have been conducted in the mixed layer with inertial oscillations, but devoid of propagating internal waves. The objective of the present numerical study is to identify the contributions of waves and vortical modes to submesoscale lateral dispersion in the stratified interior, where wave and vortical-mode energy levels are comparable. This is accomplished by performing idealized simulations under identical conditions with a set of reduced-interaction models (Remmel 2010; Hernández-Dueñas et al. 2014) that include subsets of all possible classes of nonlinear interactions. The models were first developed for shallow-water systems (Remmel and Smith 2009) and extended to rotating stratified flows by Remmel (2010) and Hernández-Dueñas et al. (2014). The current study relies on the models described in Hernández-Dueñas et al. (2014), which include the quasigeostrophic (QG) model with only vortical-mode nonlinearities, a model (P2G) with all interactions except wave–wave–wave interactions, and the full Boussinesq (FB) model that retains all possible classes of nonlinear interactions between the two components. A wave turbulence model (GGG) is also included (Remmel et al. 2010, 2014). The GGG model can be viewed as an extension of weak wave turbulence. Whereas weak wave turbulence models retain only resonant wave–wave–wave interactions (Zakharov et al. 1992; Newell and Rumpf 2011; Nazarenko 2011; McComas and Bretherton 1977; Lvov and Tabak 2004; Lvov et al. 2004, 2010), the GGG model includes all wave triads, including the nonresonant ones. The QG and GGG models are useful for studying flow evolution when only vortical modes or wave modes are separately present, whereas P2G and FB provide information on energy exchanges between the two components. We find that the presence of internal waves, through their interaction with vortical modes, leads to nonnegligible differences in lateral dispersion among the different models. Moreover, the ability to isolate classes of interactions between waves and vortical modes helps to identify and explain the role of each component in dispersion behavior.

In this study, all models are spun up from rest with identical forcing designed to represent parameterized wave-breaking events occurring at random locations in the domain. These parameterized events are introduced through enhanced localized vertical diffusivities that produce patches of well-mixed fluid. The mixed patches are out of equilibrium with the surrounding stably stratified fluid and undergo cyclogeostrophic adjustment, resulting in the spinup of a vortex structure and a radiating wave field (Lelong and Sundermeyer 2005; Sundermeyer and Lelong 2005). The models are continuously forced in this fashion until the flows reach statistical equilibrium, at which point Lagrangian particles are placed in the domain.

The broad range of temporal and spatial scales that must be resolved simultaneously render these computations very memory and time intensive. Available computational resources limit the maximum wave frequency band N/f that can be considered (parameters are defined in section 2a). Therefore, applying conclusions of our study to oceanic regions with larger N/f requires extrapolation to a dynamically similar regime obtained by preserving nondimensional Rossby and Burger numbers (e.g., Lelong and Dunkerton 1998).

The rest of the paper is organized as follows. The mathematical foundations of intermediate models are given in section 2. The numerical setup, specification of parameter values, and forcing strategy are described in section 3. Section 4 provides detailed intermodel comparisons for understanding the role of wave and vortical motions on lateral dispersion. Section 5 interprets dispersion patterns in terms of physical flow features, kinetic energy and transfer spectra. A discussion of our results is provided in section 6.

2. Model equations

a. Boussinesq dynamics

The Boussinesq approximation to the compressible fluid equations is commonly adopted to describe low-Mach-number, nonhydrostatic motions such as the turbulent velocity and density fluctuations present in the oceanic submesoscales. The Boussinesq model filters high-frequency acoustic waves while still retaining the influence of density fluctuations through the buoyancy term in the statement of conservation of momentum (Boussinesq 1877). Hence, the Boussinesq framework is a practical choice to study the interactions between moderate frequency inertia–gravity waves and so-called balanced flows, which at lowest order are the motions that exist in the absence of waves altogether and account for linear PV.

Nonlinear exchanges between these two components are often called wave–vortical interactions, in reference to the vortical nature of balanced flows. Quantitative understanding of wave–vortical interactions continues to be an important research area. Several recent theoretical and numerical studies have found that internal waves and balanced motions may interact and exchange energy (e.g., Taylor and Straub 2016; Barkan et al. 2017; Xie and Vanneste 2015; Wagner and Young 2016; Thomas and Daniel 2020), thereby impacting the accuracy of regional and global ocean–atmosphere models (Torres et al. 2018; Whalen et al. 2020).

Assuming alignment of the direction of gravity and the axis of Earth's rotation in the vertical $\hat{\mathbf{z}}$ direction, the unforced, inviscid Boussinesq equations are given by

$$\frac{D\mathbf{u}}{Dt} + f\hat{\mathbf{z}} \times \mathbf{u} = -\frac{1}{\rho_o}\nabla p - \hat{\mathbf{z}}\frac{g}{\rho_o}\rho', \tag{1a}$$

$$\frac{D\rho'}{Dt} = -w\frac{d\overline{\rho}}{dz}, \quad \text{and} \tag{1b}$$

$$\nabla \cdot \mathbf{u} = 0, \tag{1c}$$

where $\mathbf{u}(\mathbf{x}, t)$ is velocity, $\rho(\mathbf{x}, t) = \rho_o + \overline{\rho}(z) + \rho'(\mathbf{x}, t)$ is density, and $p(\mathbf{x}, t)$ is dynamic pressure. The constant ρ_o and linear function $\overline{\rho}(z) = -Bz$ describe the fixed reference state, and the constant B characterizes the density stratification. The Coriolis frequency f is taken here to be a constant, consistent with relatively small variations of f in a restricted latitude range at midlatitudes. The linearized version of system (1) with triply periodic boundary conditions is known to support propagating inertia–gravity wave solutions, as well as nonpropagating solutions sometimes referred to as "slow modes" or "vortical modes." These wave and vortical solutions may be conveniently expressed in terms of a scaled density $\theta = (B\rho_o/g)^{-1/2}\rho'$, which has dimensions of velocity, such that

$$\mathbf{\Phi}^s(\mathbf{x}, t; \mathbf{k}) = \begin{pmatrix} \mathbf{u} \\ \theta \end{pmatrix} = \boldsymbol{\phi}^s(\mathbf{k})e^{i[\mathbf{k}\cdot\mathbf{x} - \sigma^s(\mathbf{k})t]}, \tag{2}$$

where the four vectors $\mathbf{\Phi}^s(\mathbf{x}, t; \mathbf{k})$, $s = 0, +, -$ are parameterized by the wavevector $\mathbf{k}$. The eigenvectors $\boldsymbol{\phi}^s(\mathbf{k})$ can be found in, for example, Bartello (1995), Smith and Waleffe (2002), Majda (2003), and Hernández-Dueñas et al. (2014). See the appendix for more details. The superscript 0 is used to denote the vortical mode with zero-frequency $\sigma_0(\mathbf{k}) = 0$, and the superscripts $\pm$ denote the wave modes with frequencies (eigenvalues)

$$\sigma^{\pm}(\mathbf{k}) = \pm\frac{(N^2k_h^2 + f^2k_z^2)^{1/2}}{k}, \tag{3}$$

where $k = |\mathbf{k}|$ is the wavenumber corresponding to the wavevector $\mathbf{k}$, and $k_h = (k_x^2 + k_y^2)^{1/2}$ and k_z are its horizontal and vertical wavenumber, respectively. The constant buoyancy frequency N is given by $N = (gB/\rho_o)^{1/2}$, and the density fluctuation can be rewritten as $\rho' = B\theta/N$.

Completeness of the divergence-free eigenmodes $\boldsymbol{\phi}^s(\mathbf{k})$ allows for an equivalent $\mathbf{k}$-space description of the dynamics in (1) in a triply periodic domain, given by

$$\frac{\partial b^{s_\mathbf{k}}(\mathbf{k}, t)}{\partial t} = \sum_{\mathbf{k}+\mathbf{p}+\mathbf{q}=0}\ \sum_{s_\mathbf{p}, s_\mathbf{q}=0,\pm} C_{\mathbf{kpq}}^{s_\mathbf{k}s_\mathbf{p}s_\mathbf{q}}\, \overline{b^{s_\mathbf{p}}}(\mathbf{p}, t)\, \overline{b^{s_\mathbf{q}}}(\mathbf{q}, t) \exp\{i[\sigma^{s_\mathbf{k}}(\mathbf{k}) + \sigma^{s_\mathbf{p}}(\mathbf{p}) + \sigma^{s_\mathbf{q}}(\mathbf{q})]t\} \tag{4}$$

where the overbar denotes complex conjugate. The fields $\mathbf{u}$ and θ are recovered from the expansion

$$\begin{pmatrix} \mathbf{u} \\ \theta \end{pmatrix}(\mathbf{x}, t) = \sum_{\mathbf{k}} \sum_{s_\mathbf{k}=0,\pm} b^{s_\mathbf{k}}(\mathbf{k}, t)\boldsymbol{\phi}^{s_\mathbf{k}}(\mathbf{k}) \exp\{i[\mathbf{k}\cdot\mathbf{x} - \sigma^{s_\mathbf{k}}(\mathbf{k})t]\}. \tag{5}$$

Note that (4) is shorthand notation for three coupled partial differential equations, since $s_\mathbf{k}$ takes on the values $s_\mathbf{k} = 0, \pm$; three equations are sufficient (instead of four) because the eigenvectors $\boldsymbol{\phi}^s(\mathbf{k})$ are divergence free. Fourier pseudospectral codes solve (4) for the unknown amplitudes $b^s(\mathbf{k})$, taking advantage of fast Fourier transforms to compute the nonlinear term as a local product in $\mathbf{x}$ space rather than the convolution sum in $\mathbf{k}$ space. The known interaction coefficients $C_{\mathbf{kpq}}^{s_\mathbf{k}s_\mathbf{p}s_\mathbf{q}}$ are computed from the eigenmodes $\boldsymbol{\phi}^s(\mathbf{k})$ and their complex conjugates (e.g., Remmel et al. 2014).

The reduced models studied herein result from a restriction of the convolution sum in (4) to selected classes of interactions ($s_\mathbf{k}\, s_\mathbf{p}\, s_\mathbf{q}$). Each such model automatically satisfies global energy conservation because each triad ($\mathbf{k}\ \mathbf{p}\ \mathbf{q}$) separately satisfies the detailed balance relation $C_{\mathbf{kpq}}^{s_\mathbf{k}s_\mathbf{p}s_\mathbf{q}} + C_{\mathbf{qkp}}^{s_\mathbf{q}s_\mathbf{k}s_\mathbf{p}} + C_{\mathbf{pqk}}^{s_\mathbf{p}s_\mathbf{q}s_\mathbf{k}} = 0$ (Kraichnan 1973). Restriction of the convolution sum in Fourier space corresponds to a projection onto the corresponding selected wave–vortical interactions in physical space, and the models are "reduced" in the sense of the projection. For more details, see Remmel (2010) and Hernández-Dueñas et al. (2014) for the Boussinesq system and Remmel and Smith (2009) for the shallow water equations. After the projection in physical space, each reduced model is a system of partial differential equations with modified nonlinear terms.

Two of the reduced models eliminate wave–vortical interactions. On the one hand, the quasigeostrophic (QG) model consists of vortical-mode interactions in the absence of waves. On the other hand, a waves-only model considers the interactions between three inertia–gravity waves in the absence of vortical modes. The latter model was named GGG as an acronym for three (inertia)–gravity waves. These two "extreme" cases are quite different, since the QG model supports an inverse cascade of vortical-mode energy, while the GGG model mainly supports a forward cascade of wave energy in strongly stratified flows. A third reduced model includes all interactions *except* three-wave interactions, and hence highlights how wave–vortical interactions modify QG dynamics, and the spurious effects introduced by exclusion of three-wave interactions. By comparison with Boussinesq dynamics given by (1) or equivalently (4), numerical simulations with the reduced models help to clarify the different contributions of vortical, wave and mixed wave–vortical interactions in influencing both dynamics and stirring in the ocean submesoscales.

b. *The quasigeostrophic approximation*

The quasigeostrophic (QG) approximation to (1) describes the nonlinear dynamics of the vortical mode in the absence of inertia–gravity waves. The QG model was conceived for midlatitude, large-scale motions in the atmosphere and oceans, evolving on time scales that are long relative to the wave periods associated with eigenvalues (3) (Charney 1948, 1971). Among its many foundational aspects, the QG approximation provides a theoretically tractable and numerically inexpensive framework for understanding the baroclinic instability, potential vorticity dynamics, and geostrophic turbulence (Charney 1948, 1971; Pedlosky 1982; Gill 1982; Vallis 2017).

In the geophysical fluid dynamics literature, QG is usually derived from a distinguished asymptotic limiting process (Majda 2003). Main assumptions are that $\mathrm{Fr} \sim \mathrm{Ro} = \epsilon \to 0$, where the Rossby number $\mathrm{Ro} \propto 1/f$ and the Froude number $\mathrm{Fr} \propto 1/N$ are nondimensional parameters characterizing the relative strengths of rotation and stratification. Formally, the QG model may also be derived by projection of the dynamics

(4) onto the subset of vortical mode interactions $(s_{\mathbf{k}}\, s_{\mathbf{p}}\, s_{\mathbf{q}}) = (0\,0\,0)$ and exclusion of all other triad interaction types (Smith and Waleffe 2002). A mathematical proof based on fast wave averaging has rigorously established the decoupling of waves and vortical modes for $\epsilon \to 0$ (Embid and Majda 1996, 1998); see also Babin et al. (1997, 2000).

From (4), QG dynamics may be written in Fourier space as

$$\frac{\partial b^0(\mathbf{k},t)}{\partial t} = \sum_{\mathbf{k}+\mathbf{p}+\mathbf{q}=0} C^{000}_{\mathbf{kpq}}\, \overline{b^0}(\mathbf{p},t)\, \overline{b^0}(\mathbf{q},t), \tag{6}$$

with

$$\begin{pmatrix}\mathbf{u}\\ \theta\end{pmatrix}(\mathbf{x},t) = \sum_{\mathbf{k}} b^0(\mathbf{k},t)\boldsymbol{\phi}^0(\mathbf{k})\exp(i\mathbf{k}\cdot\mathbf{x}), \tag{7}$$

where we have used the fact that vortical modes have zero frequency $\sigma^0 = 0$. Although derived as an asymptotic description of scales larger than the Rossby deformation radius (approximately 50 km in the ocean at midlatitudes), QG serves as a "null hypothesis," providing an important reference model to qualitatively and quantitatively assess the importance of wave–vortical interactions.

c. The wave turbulence approximation (GGG)

A different reference point is provided by three-wave interactions, whose dynamics are given by

$$\frac{\partial b^{s_{\mathbf{k}}}(\mathbf{k},t)}{\partial t} = \sum_{\mathbf{k}+\mathbf{p}+\mathbf{q}=0}\ \sum_{s_{\mathbf{p}},s_{\mathbf{q}}=\pm} C^{s_{\mathbf{k}}s_{\mathbf{p}}s_{\mathbf{q}}}_{\mathbf{kpq}}\, \overline{b^{s_{\mathbf{p}}}}(\mathbf{p},t)\, \overline{b^{s_{\mathbf{q}}}}(\mathbf{q},t)\exp\{i[\sigma^{s_{\mathbf{k}}}(\mathbf{k}) + \sigma^{s_{\mathbf{p}}}(\mathbf{p}) + \sigma^{s_{\mathbf{q}}}(\mathbf{q})]t\}, \tag{8}$$

$$\begin{pmatrix}\mathbf{u}\\ \theta\end{pmatrix}(\mathbf{x},t) = \sum_{\mathbf{k}}\sum_{s_{\mathbf{k}}=\pm} b^{s_{\mathbf{k}}}(\mathbf{k},t)\boldsymbol{\phi}^{s_{\mathbf{k}}}(\mathbf{k})\exp\{i[\mathbf{k}\cdot\mathbf{x} - \sigma^{s_{\mathbf{k}}}(\mathbf{k})t]\}. \tag{9}$$

Equation (8) is shorthand notation for the two equations for $b^+(\mathbf{k}, t)$ and $b^-(\mathbf{k}, t)$, and the acronym GGG stands for interactions among three gravity waves. Dynamics given by GGG can be viewed as a nonperturbative extension of wave turbulence (WT) theory, which would further restrict the triad interactions in (8) to satisfy the resonance condition $\sigma^{s_{\mathbf{k}}}(\mathbf{k}) + \sigma^{s_{\mathbf{p}}}(\mathbf{p}) + \sigma^{s_{\mathbf{q}}}(\mathbf{q}) = 0$ (Zakharov et al. 1992; Newell and Rumpf 2011; Nazarenko 2011). Wave turbulence theory has been used as a model to understand the ocean internal wave spectrum (McComas and Bretherton 1977; Garrett and Munk 1979; Lvov and Tabak 2004; Lvov et al. 2004, 2010).

By including all three-wave interactions, (8) captures additional physics beyond WT theory, including the formation of vertically sheared horizontal flows (Smith and Waleffe 2002; Remmel et al. 2010, 2014; Lvov et al. 2012; Gamba et al. 2020), which are given the acronym VSHF. These are horizontal layers of uniform flow separated by vertical shear, corresponding to energy accumulation in the $k_h = 0$ wave modes.

Using numerical simulations with random forcing at small scales, Smith and Waleffe (2002) demonstrated that VSHF may dominate the large-scale flow structure in strongly stratified turbulence on long time scales. The generation of VSHF is a phenomenon associated with nonresonant three-wave interactions, because the coupling coefficient $C^{s_{\mathbf{k}}s_{\mathbf{p}}s_{\mathbf{q}}}_{\mathbf{kpq}}$ is identically zero when $k_h = 0$ in a resonant three-wave triad (Lelong and Riley 1991). For more information about VSHF, see Smith and Waleffe (2002), Waite and Bartello (2006), Laval et al. (2003), Remmel et al. (2010, 2014), Lvov et al. (2012), Fitzgerald and Farrell (2018a,b), and Gamba et al. (2020). Since vertical shear will tend to separate particles in the horizontal direction, the VSHF are expected to play a role in horizontal dispersion. Three-wave interactions are also important for transport in the vertical direction.

d. Dynamics in the absence of three-wave interactions (P2G)

The remaining model studied in this work is the projection of (1) onto the set of triad interactions that includes at least one vortical mode, given in $\mathbf{k}$ space by the equations

$$\frac{\partial b^0(\mathbf{k},t)}{\partial t} = \sum_{\mathbf{k}+\mathbf{p}+\mathbf{q}=0}\ \sum_{s_{\mathbf{p}},s_{\mathbf{q}}=0,\pm} C^{0s_{\mathbf{p}}s_{\mathbf{q}}}_{\mathbf{kpq}}\, \overline{b^{s_{\mathbf{p}}}}(\mathbf{p},t)\, \overline{b^{s_{\mathbf{q}}}}(\mathbf{q},t)\exp\{i[\sigma^{s_{\mathbf{p}}}(\mathbf{p}) + \sigma^{s_{\mathbf{q}}}(\mathbf{q})]t\}, \tag{10}$$

$$\begin{aligned}\frac{\partial b^{\pm}(\mathbf{k},t)}{\partial t} = {}& \sum_{\mathbf{k}+\mathbf{p}+\mathbf{q}=0}\ \sum_{s_{\mathbf{q}}=0,\pm} C^{\pm 0 s_{\mathbf{q}}}_{\mathbf{kpq}}\, \overline{b^{0}}(\mathbf{p},t)\, \overline{b^{s_{\mathbf{q}}}}(\mathbf{q},t)\exp\{i[\sigma^{\pm}(\mathbf{k}) + \sigma^{s_{\mathbf{q}}}(\mathbf{q})]t\} + \sum_{\mathbf{k}+\mathbf{p}+\mathbf{q}=0}\ \sum_{s_{\mathbf{p}}=0,\pm} C^{\pm s_{\mathbf{p}} 0}_{\mathbf{kpq}}\, \overline{b^{s_{\mathbf{p}}}}(\mathbf{p},t)\, \overline{b^{0}}(\mathbf{q},t)\\ &\times\exp\{i[\sigma^{\pm}(\mathbf{k}) + \sigma^{s_{\mathbf{p}}}(\mathbf{p})]t\},\end{aligned} \tag{11}$$

where (11) is shorthand for the two equations for $b^+(\mathbf{k}, t)$ and $b^-(\mathbf{k}, t)$ and the fields $\mathbf{u}$ and θ are recovered from the expansion in (5). This model was named P2G in Remmel (2010) to indicate that triad interactions may contain up to two gravity waves (hence 2G).

The dynamics of P2G allow for wave–vortical interactions to modify purely QG dynamics. In previous studies using 2π-periodic domains with aspect ratio 1 and Fr = Ro ≈ 0.1, the wave–vortical interactions were shown to be responsible for asymmetry between cyclones and anticyclones, which asymmetry is absent in QG dynamics alone (Hernández-Dueñas et al. 2014). Furthermore, the size of P2G large-scale vortices was observed to be smaller than the vortices of QG (Remmel and Smith 2009; Hernández-Dueñas et al. 2014), and hence closer to the size of vortices generated by full dynamics. The smaller size of P2G and Boussinesq vortices is linked to a modification of the QG inverse cascade by wave–vortical interactions.

Here we investigate how such dynamical effects of wave–vortical interactions change scalar transport, and in particular the effective horizontal diffusivities, in a numerical setup and parameter regime that is relevant to the ocean submesoscales.

3. Numerical setup

a. Limited N/f regime

Correctly simulating submesoscale lateral dispersion requires including simultaneously length scales that span several orders of magnitude over periods of several days, with sufficiently small time steps to resolve the buoyancy frequency. To circumvent this computational hurdle, our simulations are performed in a regime dynamically similar to typical midlatitude upper-ocean conditions but numerically more tractable. We accomplish this by increasing the Coriolis frequency f while decreasing the horizontal scale L by the same factor. Buoyancy frequency N and vertical length scale h remain fixed. Therefore, h/L is increased while N/f is decreased to preserve the Burger number $\mathrm{Bu} = [Nh/(fL)]^2$ and the underlying dynamics of the flow. This technique has proven particularly useful in a number of studies similar to this one where model spinups from rest can take hundreds of inertial periods (Lelong and Sundermeyer 2005; Sundermeyer and Lelong 2005; Brunner-Suzuki et al. 2012, 2014). Sensitivity studies have shown that for simulation times comparable to the ones presented here, results are not significantly impacted by the value of N/f (Lelong and Dunkerton 1998). The results presented in the next section were all obtained with horizontal lengths scaled down by a factor of 10, and f increased by a factor of 10. While all of our simulations are performed with $N/f = 10$, a rescaling of horizontal and time scales will enable us to relate our results to a realistic upper-ocean regime (section 5d).

b. Model parameters and definitions

All simulations are performed in a domain $D = (0, L_x) \times (0, L_y) \times (0, L_z)$, where $L_x = L_y = 500$ m and $L_z = 50$ m, with aspect ratio $L_z/L_x = 1/10$. The Coriolis frequency is $f = 9.47 \times 10^{-4}\,\mathrm{s}^{-1}$ and the Brunt–Väisäla frequency is $N = 9.47 \times 10^{-3}\,\mathrm{s}^{-1}$. The characteristic time scale is the inertial period, $\tau = 2\pi/f = 6634.8$ s $= 1.84$ h. The density background with constant stratification $\rho_o - Bz$ is given by the reference value $\rho_o = 1024\,\mathrm{kg\,m^{-3}}$, and the density stratification $B = 0.0094\,\mathrm{kg\,m^{-4}}$. The entire list of parameters and definitions is given in Table 1. The models use hyperviscosity at the smallest scales and hypoviscosity at the largest scales to control energy. Details of their implementation are included in the appendix.

c. Forcing

The flows in the four models are spun up from rest in identical fashion, with sustained forcing designed to mimic intermittent wave breaking in the ocean. Density anomalies, introduced periodically in the domain at random locations by means of a local enhanced diffusivity $\kappa(x, y, z)$, represent the parameterized end-states of wave-breaking events at the stage following isopycnal overturning, when localized mixing has occurred. Each wave-breaking event is assumed to produce a perfectly mixed patch of fluid. These patches are out of equilibrium with the background density and undergo cyclogeostrophic adjustment, producing S-vortex structures composed of a central anticyclone flanked above and below by two weaker cyclones (Morel and McWilliams 1997). In addition to the spinup of vortices, each adjustment event also excites a radiating internal wave field.

TABLE 1. Parameter values.

Parameter	Symbol	Value
Horizontal dimension	$L_x = L_y$	500 m
Vertical dimension	L_z	50 m
Coriolis parameter	F	$f = 9.47 \times 10^{-4}\,\mathrm{s}^{-1}$
Brunt–Väisälä frequency	N	$9.47 \times 10^{-3}\,\mathrm{s}^{-1}$
Characteristic time	$\tau = 2\pi/f$	6634.8 s = 1.84 h
Density background	$\rho_o - Bz$	$\rho_o = 1024\,\mathrm{kg\,m^{-3}}$; $B = 0.0094\,\mathrm{kg\,m^{-4}}$

This method of forcing was first implemented by Sundermeyer and Lelong (2005) to spin up realistic vortical and wave fields in triply periodic domains characteristic of pycnocline conditions, in the absence of wind and tidal forces. Following Sundermeyer and Lelong (2005), each anomaly is computed as the solution of an initial/boundary value problem

$$\begin{cases} \dfrac{\partial}{\partial_s}\rho_f' = \dfrac{\partial}{\partial z}\left\{\kappa_z \dfrac{\partial}{\partial_z}[\overline{\rho}(z) + \rho_f']\right\}, \\ \rho_f'|_{s=0} = 0. \end{cases} \tag{12}$$

Here ρ_f' is the density fluctuation so that $\rho_f = \rho_o + \overline{\rho}(z) + \rho_f'$, and we impose periodic boundary conditions on ρ_f'. Furthermore, the coefficient κ_z is a Gaussian function given by

$$\kappa_z(x,y,z) = 9.42 \times 10^{-2}\,\mathrm{m^2\,s^{-1}} \exp\left[-\frac{(x-x_o)^2 + (y-y_o)^2}{2r_h^2} - \frac{(z-z_o)^2}{2r_z^2}\right], \tag{13}$$

where $r_h = 12.5$ m, $r_z = 2.5$ m, and (x_o, y_o, z_o) is the center of the anomaly chosen at random locations. Each wave-breaking event is parameterized by the injection of the density anomalies ρ_f' at random locations every 0.4 inertial periods. The center (x_o, y_o, z_o) is always located on the grid and each coordinate is chosen randomly from a uniform distribution. See Figs. 1 and 4 of Sundermeyer and Lelong (2005) for visualizations of the density anomaly forcing ρ_f'.

The final state generates a well-mixed region centered about (x_o, y_o, z_o) where the density is nearly constant. Using the characteristic scales r_h and r_z, the Burger number based on the forcing is

$$\mathrm{Bu} = \frac{r_z^2 \Delta N^2}{f^2 r_h^2} = \frac{r_z^2 N^2}{f^2 r_h^2} = 4. \tag{14}$$

The ratio r_z/r_h governs the amount of energy converted to vortical and wave fields during adjustment. Choosing Bu of $O(1)$ ensures that the adjustment of each density anomaly produces comparable wave and vortical-mode energies.

We note that, by construction, the forcing described by (12) does not project onto the $k_h = 0$ modes corresponding to vertically sheared horizontal flows (VSHF). Therefore, all VSHF energy present in our simulations must result from nonlinear interactions. VSHF are of particular interest here because, coupled with vertical diffusivity, they can enhance lateral dispersion and increase effective horizontal diffusivity (e.g., Young et al. 1982).

d. Spinup to statistical equilibrium

The quasi-steady state of the flow entails a delicate balance between forcing, energy fluxes and hypo-/hyperviscous forces. The vortical and wave energies are defined as the corresponding quantities given by the vortical and wave projections of the solution, respectively, as done in (A1) in the appendix.

Vortical and wave energies as a function of time for the four models are shown in Fig. 1. All models equilibrate to quasi-statistical steady state after 200 inertial periods and are run for an additional 60 inertial periods. Steady-state vortical energies (top panel) in Boussinesq, P2G, and QG models are comparable. Wave energy (bottom panel) in the P2G model is slightly higher than in the Boussinesq system, and significantly higher in the GGG model than in the other cases. The latter may be explained by the accumulation of energy in the vertically sheared horizontal flows (VSHF modes), via off-resonant interactions. In P2G, the three-wave interactions are absent, reducing both the generation of VSHF and the forward transfer of wave energy. VSHF modes will be discussed in more detail in sections 5b and 5c.

A 3D view of the steady-state Boussinesq flow at $t = 200$ inertial periods is shown in Fig. 2. The vortices are visualized by plotting isosurfaces (red) of linear PV given by

$$\mathrm{PV} = \left(\frac{B\rho_o}{g}\right)^{1/2}(f\hat{z}\cdot\nabla\theta - N\hat{z}\cdot\boldsymbol{\omega}), \tag{15}$$

where $\boldsymbol{\omega} = \nabla \times \mathbf{u}$ is the relative vorticity. The isosurfaces in Fig. 2 correspond to the value $\mathrm{PV} = 0.5 \times 10^{-5}\,\mathrm{kg\,m^{-3}\,m^{-1}\,s^{-1}}$, and the nearby velocity field is indicated by cyan arrows. The 3D view of the fluid reveals the horizontal and vertical distribution of the vortices, with flattened vortices staggered throughout the water column. Also shown at the bottom and at the walls are contours of the linear PV, giving us a hint of the vertical structure. The color bar ($\mathrm{kg\,m^{-4}\,s^{-1}}$) corresponds to the PV contours at the walls. Outside the box, an inset shows a zoomed-in vortex along with the neighboring velocity field.

e. Lagrangian particles and effective lateral diffusivity

Following equilibration of all models to statistically steady-state, Lagrangian particles were injected into each model and tracked in time for 10τ, where τ is the inertial period. To reduce sensitivity to the initial conditions, we tracked particles starting from initial times $t = \{200, 210, 220, 230, 240, 250\}\tau$, corresponding to six different initial flow fields (see Fig. 1). In all cases, particles were placed in the entire domain, every 4 grid points in the horizontal direction and 2 grid points in the vertical direction (total number of particles $N_p = 131\,072$). The sensitivity of our results to the number of particles was investigated, and N_p was ultimately chosen because it showed good convergence with cases for which particles were placed at every grid point.

Our main result is about the effective lateral diffusivity, which can be inferred from the pairwise separation of

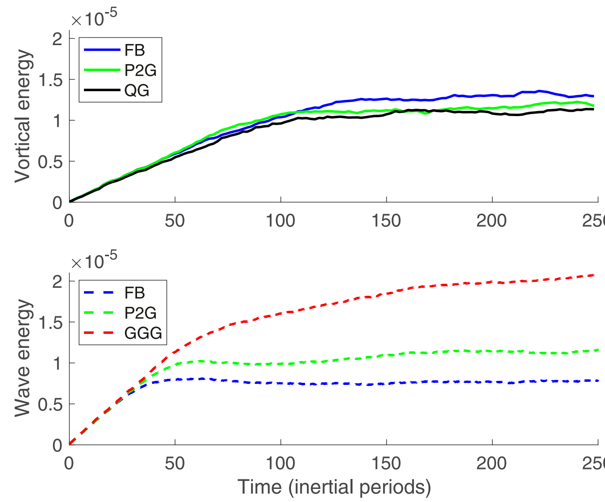

FIG. 1. Volume-averaged (top) vortical and (bottom) wave energy density ($\mathrm{m^2\,s^{-2}}$) vs time from 0 to 250 inertial periods. The time (x axis) is given in seconds and inertial periods in the top and bottom panels, respectively.

Lagrangian particles in time. Here, we define the lateral diffusivity as

$$\kappa_H = \frac{1}{2}\frac{d}{dt}R(t), \tag{16}$$

where

$$R(t) = \frac{1}{N_p - 1}\sum_{i=1}^{N_p}[(x_i - x_{\mathrm{com}})^2 + (y_i - y_{\mathrm{com}})^2] \tag{17}$$

represents the average spread of particles about their horizontal center of mass $\{x_{\mathrm{com}}(t), y_{\mathrm{com}}(t)\}$. The factor of 1/2 is due to the fact that we are dealing with relative and not absolute diffusivity (e.g., LaCasce 2008).

The spread $R(t)$ can also be expressed as the sum over all unique particle pairs

$$R(t) = \frac{1}{2N_p(N_p - 1)}\sum_{i\neq j}[x_i(t) - x_j(t)]^2 + [y_i(t) - y_j(t)]^2. \tag{18}$$

The formulation in terms of particle pairs is useful for computing scale-dependent diffusivities. Particles are first separated by initial vertical position, then particle pairs are binned according to their initial horizontal separation. The dispersion R_n at the horizontal scale corresponding to the nth bin is computed by averaging over all particle pairs in that bin and is averaged over all vertical levels. The dispersion of particle pairs in the nth bin is

$$R_n(t) = \frac{1}{2N_s(N_s - 1)}\sum_{i\neq j}[x_i(t) - x_j(t)]^2 + [y_i(t) - y_j(t)]^2, \tag{19}$$

where N_s represents the number of particles in the nth bin. In our simulations, we use 32 vertical levels with $N_s = 4096$ particles in each level. The corresponding diffusivity is then

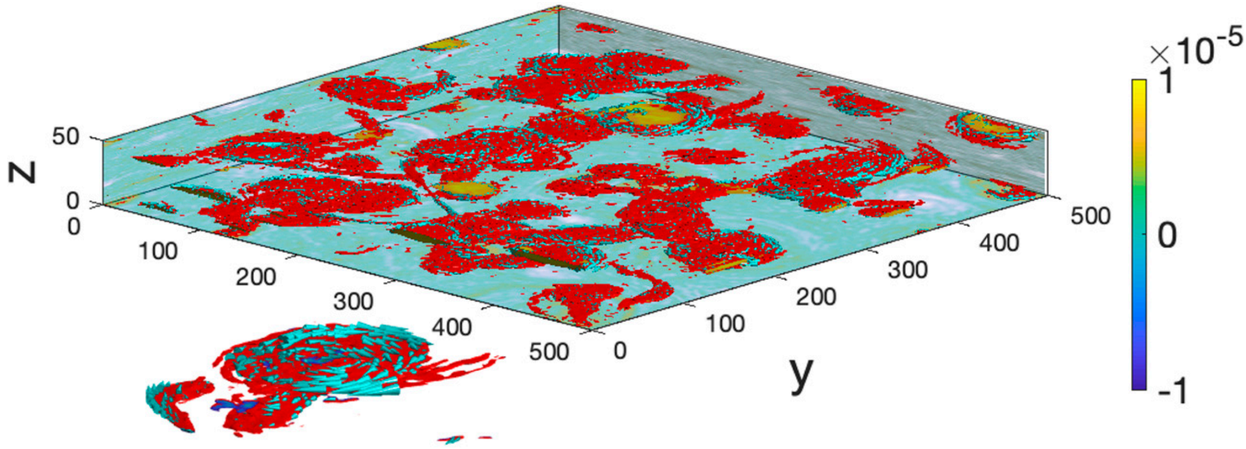

FIG. 2. A 3D view of the isosurface with linear potential vorticity value PV = 0.5×10^{-5} kg m^{-4} s^{-1} for the Boussinesq model (red isosurface). Also shown are the velocity field (cyan arrows) near the vortices and PV contours at the bottom and two of the sidewalls. The color bar (kg m^{-4} s^{-1}) corresponds to the PV contours at the walls. Outside the box, an insert shows a zoomed-in vortex with the corresponding velocity field around it. The red isosurface corresponds to anticyclones.

$$\kappa_{hn} = \frac{1}{2}\frac{dR_n(t)}{dt}. \tag{20}$$

4. Results

In this section, we contrast the evolution of Lagrangian particle trajectories in the Boussinesq (FB), P2G, QG, and GGG models described in section 2, and present the characteristics of lateral dispersion in the four models.

a. *Qualitative observations for particle dispersion*

To obtain a qualitative picture of lateral dispersion of particles in the Boussinesq system and reduced models, we present the trajectories of a few particles initially located in the center of the domain (Fig. 3). Particles are tracked during the time interval $t \in [200, 210]\tau$ and distinguished from each other using random colors. One can observe from the GGG plot (lower right) that waves-only flows are not efficient at dispersing in the horizontal plane. Particles oscillate with inertial period about their initial position, but they do not spread. The smooth trajectories in the QG model (lower left) exhibit the signature of large vortices that tend to trap particles, thereby reducing their spread. In contrast, the presence of both wave and vortical modes in FB and P2G (top panels) results in increased horizontal dispersion.

Particle trajectories in P2G and FB contain small oscillations due to the presence of waves and appear fuzzy in comparison with QG. In the case of P2G, long filaments are evident instead of the tightly wound trajectories associated with isolated vortex cores.

b. *Scale dependence of the relative diffusivity*

The scale-dependent relative diffusivity κ_H is computed from the pairwise relative separation of the particles, described in section 3e, with 32 vertical levels and 14 bins. Ensemble-averaged diffusivities and the corresponding standard error bars over the six different realizations for FB, P2G, and QG are plotted in Fig. 4. The diffusivity for GGG is an order of magnitude smaller and thus not shown. The FB, P2G, and QG model diffusivities all exhibit some scale dependence in the 0–100-m range. Beyond 100 m, the diffusivities are mostly scale-independent and asymptote to values that can be related to the absolute diffusivity, the so-called diffusive regime (LaCasce 2008; Beron-Vera and LaCasce 2016). Maximum values of κ_H (m^2 s^{-1}) are 4.2×10^{-2} for P2G, 3.6×10^{-2} for FB, and 3.4×10^{-2} for QG.

One can see that QG with vortical modes only gives an underestimate for κ_H associated with FB, where latter can be considered as the "truth model." On the other hand, there is an overestimate of approximately 17% in the P2G model, which includes the effects of wave–vortex interactions, but excludes three-wave interactions. These results point to the importance of including both vortical and wave motions in establishing correct diffusivity estimates. In particular, we will show that a key factor is the forward transfer of energy to the vortical mode by interaction with waves. Note that only off-resonant interactions can transfer energy from the wave field to the vortical mode (Lelong 1989; Bartello 1995). The impact of each class of nonlinear interactions is examined in more detail in section 5.

c. *Dispersion of purely Lagrangian versus diffusive particles*

We also performed a set of simulations with vertically diffusive particles, i.e., particles whose Lagrangian trajectories are altered slightly at each time step by the addition of a weak random-noise component in the vertical direction. In these simulations, particle displacements are designed to mimic the behavior of a diffusive dye. Figure 5 contrasts the dispersion of nondiffusive and vertically diffusive particles as a function of time in the full Boussinesq FB and waves-only GGG models (QG and P2G models are not shown because their behavior is qualitatively similar to that of FB). Corresponding diffusivities are proportional to the slopes of $R(t)$, as shown in (16).

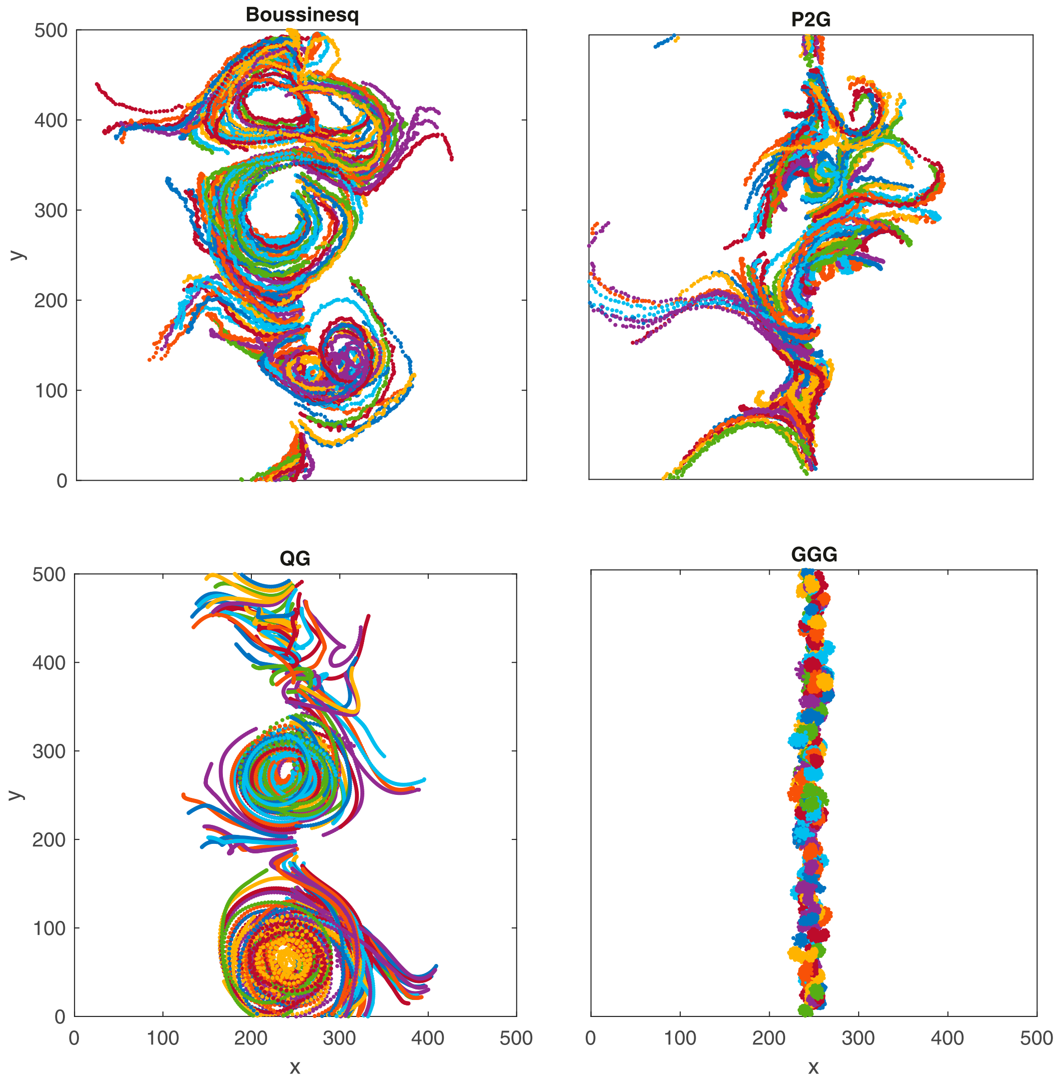

FIG. 3. Horizontal trajectories of particles marked by different colors, at time $t = 10\tau$ after particle injection. For visualization purposes, only trajectories of a few particles originally located in a strip of domain centered about $x = 250$ m, $z = 25$ m are shown.

The difference in the rate of particle dispersion with and without noise is quite pronounced in the GGG model (right panel). In the absence of noise, the particles retain their initial vertical position. Their trajectories are nearly circular with near-inertial period, as seen in the lower-right panel of Fig. 3. The small oscillations in the no-noise case (blue line in right panel) are indicative of this behavior and the effective horizontal diffusivity κ_H, proportional to the slope of the horizontal dispersion, is negligible. With the addition of noise (red dashed line in right panel), the particles diffuse vertically, then they are subjected to internal-wave shear dispersion (Young et al. 1982; see section 5c for interpretation details). The combined effect of vertical diffusion and shear enhances horizontal displacements and the estimate for the effective horizontal diffusivity from (16) is $\kappa_H = 2.1 \times 10^{-3}\,\mathrm{m^2\,s^{-1}}$ for GGG with noise. In contrast, the addition of noise does not appreciably change the rate of dispersion in FB (left panel), wherein $\kappa_H = 0.037 \times 10^{-2}\,\mathrm{m^2\,s^{-1}}$ is an order of magnitude larger than in GGG. Note that the value of κ_H in Boussinesq obtained from the slope of $R(t)$ matches the value of κ_H in the scale-independent range of Fig. 4. While internal-wave shear dispersion may be present, we conjecture that more efficient dispersion mechanisms linked to the presence of vortical modes dominate dispersion patterns in the full Boussinesq system, as will next be explained.

5. Interpretation in terms of flow fields

Physical flow features and vortical/wave kinetic energy spectra are now examined in order to explain the differences in the dispersion patterns of the four models. The goal is to

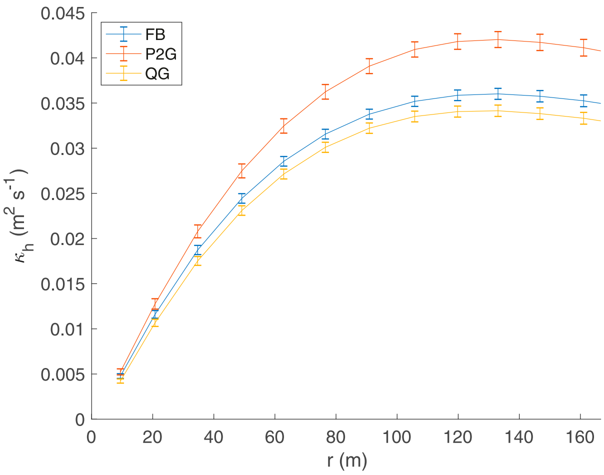

FIG. 4. Ensemble-averaged relative diffusivity with standard error vs horizontal scale for FB (blue), P2G (red), and QG (yellow). The computation is carried out according to the description in section 3e. Only pairs separated by, at most, 1/3 of the periodic domain are used.

identify the impact of waves, vortical modes, and their interactions on lateral dispersion.

a. *Linear potential vorticity fields*

The QG, P2G, and full Boussinesq models allow for inverse energy transfer to large-scale vortices through vortical-mode interactions. In our simulations, this inverse transfer is arrested by hypoviscosity confined to act on the largest scales in the domain. The statistically steady vortex fields are compared by examining linear PV contours in the horizontal plane at fixed time and height $z = 25$ m, shown in Fig. 6. In the Boussinesq model (top left), the fluid motion is dominated by a few large-scale, anticyclonic vortices (bright yellow), along with some medium-scale cyclonic vortices (dark blue). Inertia–gravity waves and fine-grained features are visible in between the vortex cores, but do not appear to disrupt the strongest and largest anticyclones. In the P2G reduced model (top left), wherein three-wave interactions are removed from the Boussinesq system, vortex cores are less well defined and disorganized small-scale structure is present. In contrast, the QG model (bottom) shows tight vortices and filaments with smoother contours and is devoid of fine-grained structure.

The PV centroid can help to quantify the above qualitative statements, defined as

$$\text{PV-Cent}(t) = \frac{\sum_{\mathbf{k}\neq 0} \sqrt{k_h^2 + \frac{f^2}{N^2} k_z^2} |\text{PV}_\mathbf{k}|^2}{\sum_{\mathbf{k}\neq 0} |\text{PV}_\mathbf{k}|^2}, \tag{21}$$

where $\text{PV}_\mathbf{k}$ is the Fourier coefficient of (15) at wavevector $\mathbf{k}$. The stretching factor $(f/N)^2$ is motivated by the dynamical equation for linear PV (Vallis 2017), and accounts for the small aspect ratio. In strongly rotating fluids, (21) is a quantity associated with the wavenumber of emerging PV vortices, with corresponding length scale

$$L_{\text{PV}} = \frac{2\pi}{\text{PV-Cent}}. \tag{22}$$

In our setup, the value of L_{PV} reflects both the size of the large-scale vortices *and* the amount of vortical mode energy at intermediate-to-small scales, where the latter is not associated with coherent structures. At time $t = 200\tau$ (200 inertial periods), L_{PV} for FB, P2G, and QG takes the approximate values 30, 15, and 49 m, respectively, consistent with the physical fields in Fig. 6 and the spectra presented in the next section.

b. *Kinetic energy spectra*

Further insight into the differences between the models is provided by examining energy spectra. Here we focus on

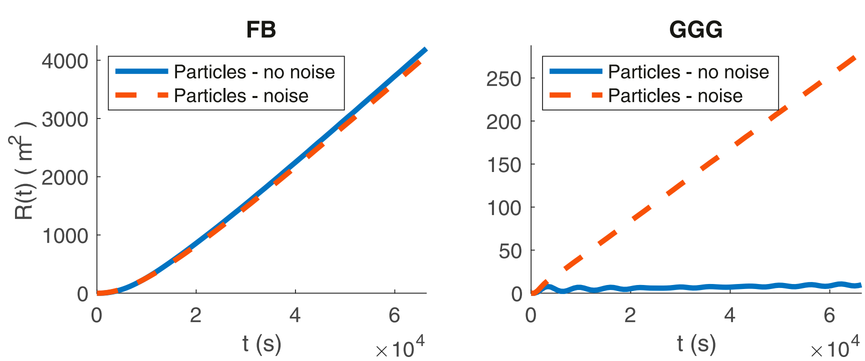

FIG. 5. Horizontal dispersion $R(t)$ [(16)], for particles without noise (blue) and with noise (dashed red) in (left) FB and (right) GGG, ensemble-averaged over six different realizations. There is a relatively small difference between the two cases for the full Boussinesq model. For the GGG model with only three-wave interactions, the no-noise particles show negligible dispersion, consistent with the small horizontal oscillations seen in the bottom-right panel of Fig. 3. In contrast, the random-walk displacements introduced by the noise produce weak linear growth of the variance $R(t)$. Note the order-of-magnitude difference between FB and GGG dispersions.

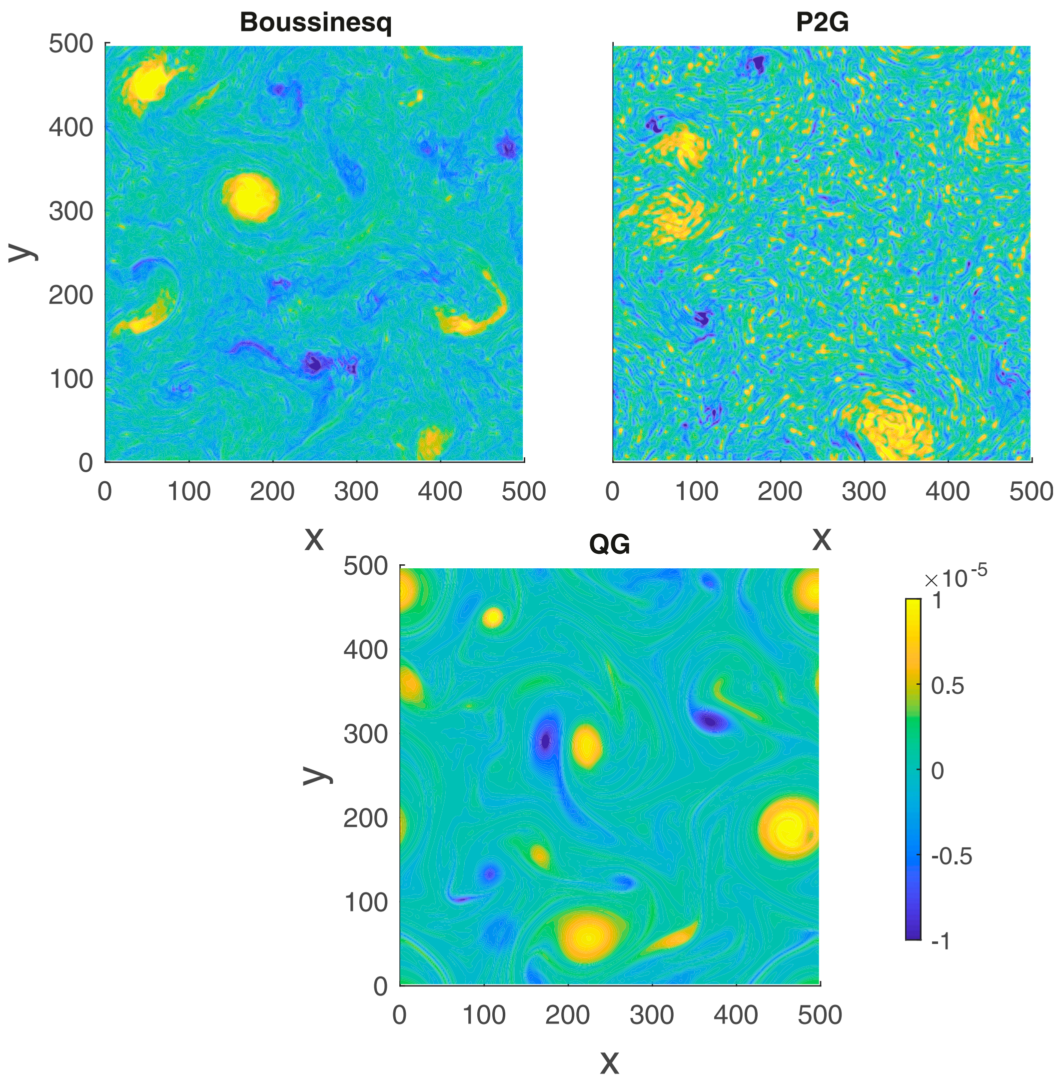

FIG. 6. Horizontal contours of the linear potential vorticity (kg m^{-4} s^{-1}) given by (15) at height $z = 25$ m and time $t = 200\tau$ for (top left) Boussinesq, (top right) P2G, and (bottom) QG. Linear PV associated with anticyclones is yellow, and that associated with cyclones is blue.

kinetic energy (Fig. 7) to inform the discussion on particle transport, though complementary information can be extracted from potential energy.

The left panel of Fig. 7 shows kinetic energy spectra as a function of horizontal wavenumber k_h, averaged over vertical wavenumber k_z, and projected onto wave and vortical components. Similarly, the right panel indicates the spectral dependence on vertical wavenumber k_z, averaged over horizontal wavenumber k_h. Horizontal wavelength λ_h and vertical wavelength λ_z in meters are displayed on the top left axis and top right axis, respectively, and we remind the reader that oceanic values for wavelengths may be extrapolated from multiplication by a factor of 10. The forcing spectra are also shown (dotted lines on each panel), where the forcing energy saturates through random injections of density anomalies as described in section 3c. Notice that the impact of the anomaly forcing is strongest for horizontal scales $50 < \lambda_h < 100$ m and vertical scales $10 < \lambda_z$ 15 m.

For small scales in our numerical setup and parameter regime, both panels of Fig. 7 show the dominance of wave-mode kinetic energy (dashed lines) over vortical-mode kinetic energy (solid lines). When waves are present (FB, P2G, and GGG), one sees that the horizontal wave spectra are surprisingly robust in the forward transfer range $10 < k_h < 70$ ($8 < \lambda_h < 100$ m), with rough scaling $k_h^{-2.5}$ (dashed lines on the left panel).

At large horizontal scales $\lambda_h > 100$ m, the GGG wave energy is dramatically elevated owing to inverse transfer into large-scale VSHF modes (see Fig. 8). Integrated over the time period $0 \le t \le \tau$, the total VSHF energy is approximately 1.2×10^{-8} m^2 s^{-2} for FB, 3.8×10^{-9} m^2 s^{-2} for P2G, and 3.4×10^{-7} m^2 s^{-2} for GGG, clearly indicating dominance of VSHF in GGG relative to the other models. Further spectral analysis shows that the GGG VSHF are most pronounced at large horizontal scales and intermediate vertical

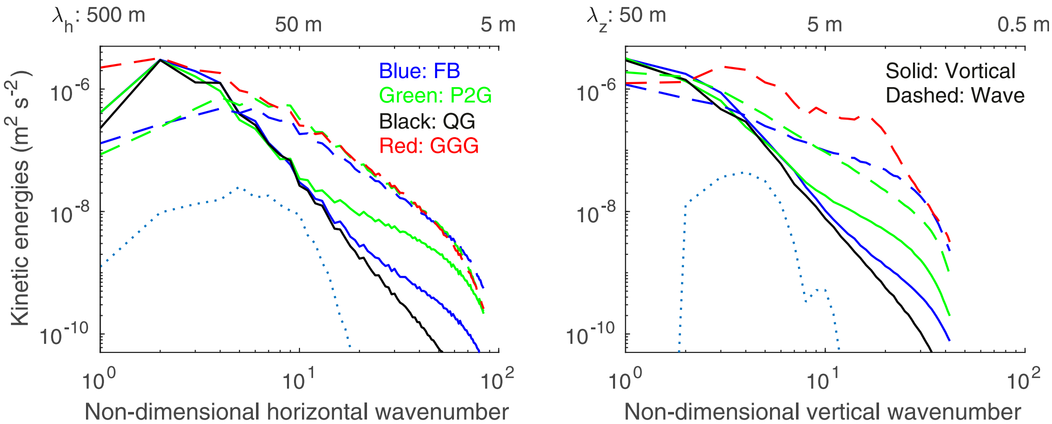

FIG. 7. Kinetic energy ($E^0_{h,\mathrm{kin}}$ and $E^{\pm}_{h,\mathrm{kin}}$) as a function of nondimensional (left) horizontal and (right) vertical wavenumber. In each panel, the energy is split into vortical (solid lines) and wave (dashed lines) for the FB (blue), P2G (green), QG (black), and GGG (red) models. The forcing spectra of density anomalies (dotted lines) are also shown. Horizontal and vertical nondimensional wavenumbers are scaled with Δk_h and Δk_z, respectively (see the appendix for details). The wavelength (m) is also provided along the upper axes.

scales, consistent with the GGG layering observed on the bottom panel of Fig. 8.

The wave kinetic energy is also dominant for vertical wavenumbers $k_z > 3$ corresponding to wavelengths $\lambda_z < 10$ m (dashed lines on the right panel of Fig. 7). For these intermediate vertical scales, a notable feature of the figure is the striking amplitude difference between the truth model FB (blue dashes) and the waves-only model GGG (red dashes). Thus, one can see that wave–vortical energy exchanges are especially important for establishing accurate wave-energy levels in vertical small scales. Furthermore, from the GGG kinetic energy spectra, it is clear that wave–wave–wave interactions support a robust forward cascade of kinetic energy.

On the other hand, when the vortical mode is present (FB, P2G, and QG), the vortical-mode kinetic energy dominates at large horizontal scales $\lambda_h \gtrsim 100$ m and large vertical scales

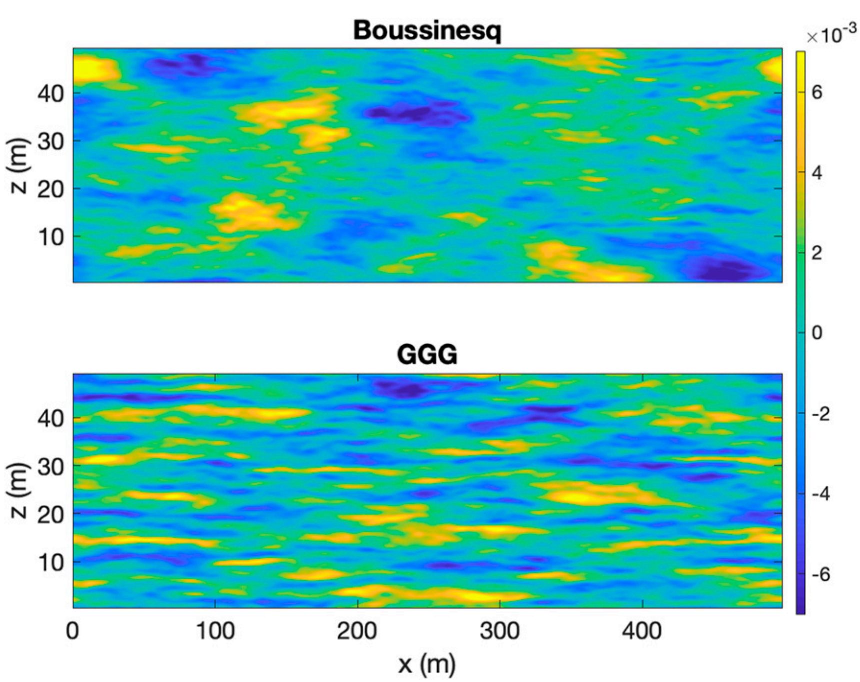

FIG. 8. Vertical slices of meridional velocity υ (m s^{-1}) for (top) Boussinesq and (bottom) waves-only GGG at $t = 200\tau$. As compared with Boussinesq, GGG has a well-defined layered structure, indicative of strong vertical shear on scales of 10 m. This is consistent with the presence of internal-wave shear dispersion, seen in Fig. 5.

$\lambda_z \gtrsim 25$ m (solid lines on both panels of Fig. 7). Large-scale, linear PV vortices are generated by vortical-mode triad interactions, as visualized in Fig. 6. Relative to QG, the horizontal slices in Fig. 6 corresponding to FB and P2G exhibit smaller-scale PV structures and the appearance of a granular background that is mostly absent in QG. These small-scale features are attributed to the presence of waves in FB and P2G, manifested in high-amplitude wave spectra at small scales, as well as higher-amplitude vortical-mode spectra at small scales (Fig. 7).

Through wave–vortical interactions, the waves in FB and P2G have the effect of increasing vortical-mode kinetic energy at small scales (blue and green solid lines in both panels of Fig. 7), relative to QG (black solid lines). One can see that the vortical-mode spectra for FB, P2G and QG are closely aligned for scales $k_h < 10$, but then diverge for $k_h > 10$. The QG model maintains a steep slope for all horizontal wavenumbers $k_h > 4$, while the FB and P2G models develop shallower vortical mode spectra for $k_h > 10$. The steep vortical-mode spectrum of QG (black solid) is associated with stirring by large-scale vortices. The shallower vortical-mode spectra for $k_h > 10$ in FB and P2G are linked with an additional contribution to stirring by smaller-scale structures that are not present in QG, and this effect is especially pronounced in the case of P2G.

Of the three models with vortical modes, P2G has the highest vortical-mode energy in small scales (green solid lines on both panels of Fig. 7), consistent with the small-scale features observed in the horizontal slice of P2G PV (the P2G panel of Fig. 6). Further understanding is provided by analysis of kinetic energy transfer in vortical–wave–wave (VWW) triads, which exist only in the FB and P2G models. Here the dash in VWW specifies that we are measuring the energy transferred into the vortical mode V from interactions between two waves WW, as confirmed in Fig. 9 (blue for FB and green for P2G). To focus on energy transfer into small horizontal scales, Fig. 9 displays variance-preserving VWW transfer spectra as a function of horizontal wavenumber k_h, and scaled by k_h (e.g., Thomson and Emery 2014). An analogous plot (not shown) produces similar behavior of VWW transfer spectra as a function of vertical wavenumber k_z. One can see that VWW energy transfer into small-scale vortical modes is strongest in P2G, in agreement with the higher level of small-scale vortical energy in Figs. 6 and 7. Since WWW interactions do not exist in P2G, the VWW interactions must absorb more forward energy transfer, as compared with FB containing both VWW and WWW. Note that, in contrast to the subclass of resonant VWW interactions, nonresonant VWW interactions can transfer energy from waves into the vortical mode, as demonstrated here. In exactly resonant interactions involving one vortical mode and two waves, Lelong (1989) and Bartello (1995) showed that the vortical mode acts as a catalyst for energy exchange between the waves. In other words, for VWW interactions, exact resonances conserve linear PV, but nonresonances do not.

c. Vertically sheared horizontal flows and wave-induced shear dispersion

Vertically sheared horizontal flows (e.g., Smith and Waleffe 2002; Fitzgerald and Farrell 2018a,b) correspond to the $k_h = 0$ wave modes and are of special interest in determining whether the mechanism of internal-wave shear dispersion contributes significantly to horizontal diffusivity. Vertical cross sections of meridional velocity v are displayed in Fig. 8 for the Boussinesq and GGG models ($t = 200$ inertial periods). The presence of layers in GGG shows that VSHF are a dominant component in the waves-only model, with corresponding shear on vertical scales of approximately 10 m.

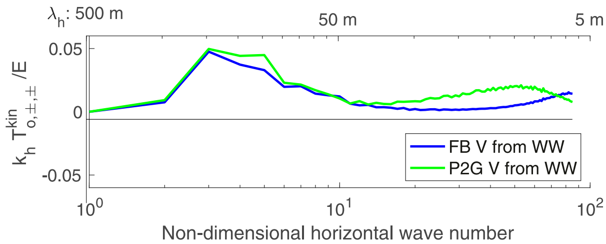

FIG. 9. Variance-preserving kinetic energy transfer spectra $k_h T^{\mathrm{kin}}_{o,\pm,\pm}/E$ as computed in (A10) for the vortical–wave–wave triad interactions, as a function of horizontal wavenumber, for the Boussinesq and P2G models. The transfer spectra are averaged over 20 inertial periods and scaled by the steady-state energy E of each model.

The strong VSHF signature in GGG confirms our conjecture that the enhanced horizontal dispersion of noisy particles is due to the combined action of vertical diffusivity and internal-wave vertical shear (Fig. 5). Consider neighboring particles at a fixed value of height z. When a small, random vertical displacement of particles is introduced at each time step by a vertical noise term, such particles may find themselves in close-by regions of oppositely signed horizontal velocity. Thus, they will immediately be separated in the horizontal direction, resulting in horizontal dispersion.

In contrast, Fig. 8 does not indicate strong horizontal layering in the Boussinesq model. There is less transfer to VSHF in Boussinesq relative to GGG because the inclusion of wave–vortex interactions provides additional forward-cascading pathways. Thus the addition of small-amplitude vertical noise to particle trajectories leads to a relatively small effect on the horizontal dispersion measured in Fig. 5.

d. Implications for the N/f = 100 regime

Our simulations are idealized in many ways, including periodic boundary conditions, limited N/f, and model forcing by density anomalies in the absence of other forcing mechanisms (tides, wind, topography, etc.). These idealizations help to isolate fundamentals of the wave–vortical interactions that are not accessible in the real ocean. On the other hand, their value for understanding the ocean is gained by connection to oceanic space and time scales, as much as possible.

Results obtained with $N/f = 10$ are related to the $N/f = 100$ upper-ocean regime by multiplying horizontal and temporal scales by 10. Hence, the diffusivities plotted in Fig. 4 correspond to scales up to 1.7 km and range in value in the scale-independent regime from $0.34 \pm 0.007\ \mathrm{m^2\,s^{-1}}$ for QG to $0.42 \pm 0.01\ \mathrm{m^2\,s^{-1}}$ for P2G, with the FB value in between at $0.36 \pm 0.007\ \mathrm{m^2\,s^{-1}}$. Considering FB to represent the truth, we find that the excess of small-scale vortical motions in the P2G model overestimates the diffusivity while the vortical-mode deficit in QG underestimates it. For comparison, comparable values ranging from 0.2 to 3 $m^2 s^{-1}$ (linked to uncertainties in the background strain rate and time dependence) were reported by Sundermeyer et al. (2020b) during the LatMix 2011 summertime experiment in the Sargasso Sea.

6. Discussion and conclusions

We have examined the role of waves and vortical modes in influencing horizontal diffusivity on $O(1)$ km scales in the ocean, by performing a suite of idealized simulations using reduced-interaction models. These models have proven informative for isolating the different contributions to lateral dispersion of waves, vortical modes, and wave–vortical interactions.

Our study focused on flows with significant wave energy (Bu = 4) that are characteristic of much of the ocean away from strong mesoscale activity. In this regime, our simulations have demonstrated that while vortical motions are primarily responsible for the Lagrangian particle dispersion patterns, the impact of waves cannot be discounted. While it has been shown that waves have little or no impact on dispersion (Balwada et al. 2021), we find that they play an indirect but nonnegligible role since their presence helps establish the spectral distribution of steady-state vortical-mode fields. In flows devoid of waves (QG), the large-scale vortices are too dominant relative to the truth model (Boussinesq), while in the absence of wave triads (P2G), the vortical flow has too much small-scale structure. In both P2G and Boussinesq models, the small-scale vortical flow remains unorganized with no evidence of vortex core formation.

Furthermore, our study provides an explanation for the development of a forward cascade and enhanced dissipation in the balanced flow, in the presence of significant wave energy, as reported in Thomas and Daniel (2021). Whereas resonant VWW interactions cannot transfer energy between wave and vortical-mode fields (Lelong 1989; Bartello 1995), it is the subclass of nonresonant VWW that is responsible for energy exchanges from the waves to smaller-scale vortical modes. In addition, the class of three-wave interactions is instrumental in setting correct dissipation rates, as seen for example in the lower wave energy levels in Boussinesq than in P2G (see Fig. 1). The indirect role of internal waves on lateral dispersion through their influence in shaping the vortical-mode spectrum is generally consistent with the conclusions of Sinha et al. (2019). These authors report that filtering out inertia–gravity waves significantly underestimates the lateral dispersion at submesoscales, with little impact on mesoscale dispersion. Our results are also in agreement with Polzin and Ferrari (2004), who concluded that vortical mode stirring was the likely source of submesoscale dispersion observed in NATRE.

A comparison of diffusivities computed from purely Lagrangian and diffusive (noisy) particle trajectories demonstrates that, in waves-only GGG flows, the effective diffusivity is due solely to internal-wave shear dispersion via the formation of VSHF flows. However, this mechanism by itself is inefficient and leads to comparatively weak effective diffusivities. In the other models with waves (P2G and FB), different triad interactions dominate the energy transfers, notably the VWW triads that are responsible for downscale energy transfer from waves to vortical modes.

The diverging slopes of vortical-mode kinetic energy spectra at small scales in Fig. 7 (left panel) suggests that an interpretation of our results in terms of local or nonlocal behavior may be subtle. At large horizontal scales, the kinetic energy spectra in all models have the same steep slope (excluding GGG, which has no vortical modes). In QG, the slope does not change appreciably from its large-scale behavior and remains greater than −3 for all wavenumbers $k_h > 4$. In contrast, for FB (P2G), the spectrum becomes noticeably shallower with slope close to (less than) −3 for $k_h > 10$. The change in slope at $k_h \approx 10$ in FB and P2G makes it difficult to distinguish whether the stirring of small scales is predominantly by large scales (nonlocal), or predominantly by comparable scales (local). In fact, it is likely that both mechanisms are important. We note that the diffusivities in Fig. 4 do not exhibit the power-law scale dependence for $r \approx$ 10–100 m predicted by Bennett (1984) for local and nonlocal regimes. The latter is perhaps not surprising, at least for FB and P2G, since Bennett's theory was developed for flows without waves.

Diffusivity due to spurious generation of PV was found in Boussinesq numerical simulations initialized with a broadband internal wave field (Bühler et al. 2013) and a Garrett–Munk spectrum (Sundermeyer et al. 2020a). In these two studies focused exclusively on waves, the generation of vortical modes (PV) by dissipative forces was found to dominate the dispersion. Unphysical production of PV at the grid scale in large-eddy simulations is also reported by Bodner and Fox-Kemper (2020). Addressing the impact of this possible additional source of diffusivity is beyond the scope of the present study but it will be investigated in the future with a detailed PV budget analysis.

Last, we recognize that the range of spatial scales considered in this idealized study is limited. Future directions will include performing simulations in larger domains capable of encompassing a greater range of scales, maintaining the resolution and gradually increasing the internal-wave frequency band N/f to include a broader internal wave spectrum in order to assess the impact of this parameter. Another promising line of research extends the constant-stratification wave/vortex decomposition used in the present study to cases with arbitrary stratification (Early et al. 2021). Numerical implementation of this generalized wave–vortex decomposition will allow extension of the simulations presented here, to vertically bounded domains with arbitrary stratification and inclusion of wind and tidal forcing.

Acknowledgments. Discussions with Jeffrey Early, Miles Sundermeyer, Eric Kunze, Cimarron Wortham, and Baylor Fox-Kemper and his group greatly improved the scope of this study. We also thank two anonymous reviewers and Joseph Fitzgerald for careful reading of our paper and helpful comments. This research was supported, in part, by Grant UNAM-DGAPA-PAPIIT IN113019 and Conacyt A1-S-17634 (Investigación realizada gracias al Programa UNAM-DGAPA-PAPIIT IN113019 and Conacyt A1-S-17634). Some simulations were performed at the Laboratorio Nacional de Visualización Científica Avanzada at UNAM Campus Juriquilla, and author Hernández-Dueñas received technical support from Luis Aguilar, Alejandro De León, and Jair García from that laboratory. Support for author Lelong was provided by NSF-OCE1536747.

Data availability statement. The numerical model simulations upon which this study is based are too large to archive. The velocity and density data at 200 inertial periods as well as the data for the particles' trajectories from 200 to 210 inertial periods are available online (https://paginas.matem.unam.mx/gerardo).

APPENDIX

Definition of Energy Spectra and Hypo- and Hyperviscosity

a. Definition of energy spectra

Each vector function $(\mathbf{u}, \theta)$ with divergence-free velocity can be decomposed as in (5). Based on that decomposition, we can define the projection of the solution into the vortical and wave modes respectively as

$$\begin{pmatrix}\mathbf{u}\\ \theta\end{pmatrix}^0(\mathbf{x},t) = \sum_{\mathbf{k}} b^0(\mathbf{k},t)\boldsymbol{\phi}^0(\mathbf{k})\exp\{i[\mathbf{k}\cdot\mathbf{x} - \sigma^0(\mathbf{k})t]\},$$
$$\begin{pmatrix}\mathbf{u}\\ \theta\end{pmatrix}^{\pm}(\mathbf{x},t) = \sum_{\mathbf{k}} b^+(\mathbf{k},t)\boldsymbol{\phi}^+(\mathbf{k})\exp\{i[\mathbf{k}\cdot\mathbf{x} - \sigma^+(\mathbf{k})t]\},$$
$$+\sum_{\mathbf{k}} b^-(\mathbf{k},t)\boldsymbol{\phi}^-(\mathbf{k})\exp\{i[\mathbf{k}\cdot\mathbf{x} - \sigma^-(\mathbf{k})t]\}, \quad \text{(A1)}$$

with

$$a^{s_\mathbf{k}}(\mathbf{k},t) := b^{s_\mathbf{k}}(\mathbf{k},t)e^{-i\sigma^{s_\mathbf{k}}(\mathbf{k})} = [\hat{\mathbf{u}}(\mathbf{k},t), \hat{\theta}(\mathbf{k},t)]\cdot\overline{\boldsymbol{\phi}^{s_\mathbf{k}}(\mathbf{k})},$$
$$s_\mathbf{k} = 0, \pm, \quad \text{(A2)}$$

where $\hat{f} = \mathcal{F}(f)$ is the discrete Fourier transform.

Here, the eigenfunctions are given by

$$\boldsymbol{\phi}^+ = \begin{cases} \dfrac{1}{\sqrt{2}\sigma k}\begin{bmatrix} \dfrac{k_z}{k_h}(\sigma k_x + ik_y f) \\ \dfrac{k_z}{k_h}(\sigma k_y - ik_x f) \\ -\sigma k_h \\ -iNk_h \end{bmatrix} & \text{if} \quad k_h \neq 0, \\ \begin{pmatrix} \dfrac{1+i}{2} \\ \dfrac{1-i}{2} \\ 0 \\ 0 \end{pmatrix} & \text{if} \quad k_h = 0, \end{cases} \quad \text{(A3)}$$

$\boldsymbol{\phi}^- = \overline{\boldsymbol{\phi}^+}$, and

$$\boldsymbol{\phi}^0 = \frac{1}{\sigma k}\begin{pmatrix} Nk_y \\ -Nk_x \\ 0 \\ fk_z \end{pmatrix}, \quad \text{(A4)}$$

where $\sigma^{s_\mathbf{k}}(\mathbf{k})$ is given by (3), $\sigma = |\sigma^{\pm}(\mathbf{k})|$, $k_h^2 = k_x^2 + k_y^2$, and $k^2 = k_x^2 + k_y^2 + k_z^2$.

The horizontal and vertical shells in Fourier space at horizontal wavenumber $\tilde{k}_h$th and vertical wavenumber $\tilde{k}_z$ are the sets

$$S_h(\tilde{k}_h) = \left\{\mathbf{k} \in \Delta k_x\mathbb{Z}\times\Delta k_y\mathbb{Z}\times\Delta k_z\mathbb{Z} : \tilde{k}_h - \frac{1}{2}\Delta k_h \le k_h \le \tilde{k}_h + \frac{1}{2}\Delta k_h\right\}, \quad \text{(A5)}$$

and

$$S_v(\tilde{k}_z) = \left\{\mathbf{k} = (k_x, k_y, k_z) \in \Delta k_x\mathbb{Z}\times\Delta k_y\mathbb{Z}\times\Delta k_z\mathbb{Z} : \tilde{k}_z - \frac{1}{2}\Delta k_z \le |k_z| \le \tilde{k}_z + \frac{1}{2}\Delta k_z\right\}, \quad \text{(A6)}$$

where $\Delta k_h = 2\pi/L_h$, $L_h = 500$ m, $\Delta k_z = 2\pi/L_z$, and $L_z = 50$ m.

The spectra as a function of horizontal and vertical wavenumber are computed as the graphs in log–log scale of the following quantities. The vortical kinetic energy as a function of horizontal $[E^0_{h,\mathrm{kin}}(\tilde{k}_h)]$ and vertical $[E^0_{v,\mathrm{kin}}(\tilde{k}_z)]$ wavenumbers, and the wave kinetic energy as a function of horizontal $[E^{\pm}_{h,\mathrm{kin}}(\tilde{k}_h)]$ and vertical $[E^{\pm}_{v,\mathrm{kin}}(\tilde{k}_z)]$ are defined respectively as

$$E^0_{h,\mathrm{kin}}(\tilde{k}_h) = \sum_{\mathbf{k}\in S_h(\tilde{k}_h)} \left(|u^0_\mathbf{k}|^2 + |v^0_\mathbf{k}|^2 + |w^0_\mathbf{k}|^2\right),$$
$$E^0_{v,\mathrm{kin}}(\tilde{k}_z) = \sum_{\mathbf{k}\in S_v(\tilde{k}_z)} \left(|u^0_\mathbf{k}|^2 + |v^0_\mathbf{k}|^2 + |w^0_\mathbf{k}|^2\right),$$
$$E^{\pm}_{h,\mathrm{kin}}(\tilde{k}_h) = \sum_{\mathbf{k}\in S_h(\tilde{k}_h)} \left(|u^{\pm}_\mathbf{k}|^2 + |v^{\pm}_\mathbf{k}|^2 + |w^{\pm}_\mathbf{k}|^2\right),$$
$$E^{\pm}_{v,\mathrm{kin}}(\tilde{k}_z) = \sum_{\mathbf{k}\in S_v(\tilde{k}_z)} \left(|u^{\pm}_\mathbf{k}|^2 + |v^{\pm}_\mathbf{k}|^2 + |w^{\pm}_\mathbf{k}|^2\right). \quad \text{(A7)}$$

Similarly, the spectra of the potential energy are defined as

$$E^0_{h,\mathrm{pot}}(\tilde{k}_h) = \sum_{\mathbf{k}\in S_h(\tilde{k}_h)} |\theta^0_\mathbf{k}|^2, \quad E^0_{v,\mathrm{pot}}(\tilde{k}_z) = \sum_{\mathbf{k}\in S_v(\tilde{k}_z)} |\theta^0_\mathbf{k}|^2,$$
$$E^{\pm}_{h,\mathrm{pot}}(\tilde{k}_h) = \sum_{\mathbf{k}\in S_h(\tilde{k}_h)} |\theta^{\pm}_\mathbf{k}|^2, \quad E^{\pm}_{v,\mathrm{pot}}(\tilde{k}_z) = \sum_{\mathbf{k}\in S_v(\tilde{k}_z)} |\theta^{\pm}_\mathbf{k}|^2. \quad \text{(A8)}$$

b. Energy transfer spectra

In the absence of hypo- and hyperviscosity, the kinetic energy $e_{\mathrm{kin}} = (1/2)u^2 + (1/2)v^2 + (1/2)w^2$ satisfies the equation

$$\frac{\partial \frac{1}{2}\|\mathbf{u}\|^2_{L^2(x)}}{\partial t} = -\langle\hat{u}, \mathscr{F}[\nabla\cdot(u\mathbf{u})]\rangle_{L^2} - \langle\hat{v}, \mathscr{F}[\nabla\cdot(v\mathbf{u})]\rangle_{L^2} - \langle\hat{w}, \mathscr{F}[\nabla\cdot(w\mathbf{u})]\rangle_{L^2} - N\langle\hat{w}, \hat{\theta}\rangle_{L^2}, \quad \text{(A9)}$$

where $\langle,\rangle_{L^2}$ is the L^2 normalized inner product in Fourier space. The first three terms in (A9) correspond to energy transfer terms and can be associated to triads as follows. Given a triad (s_1, s_2, s_3) where each s_j corresponds to either a vortical (0) or wave ($\pm$) mode, the kinetic energy transfer from (s_2, s_3) interactions into the s_1 mode at wavenumber $\mathbf{k}$ is quantified as

$$\begin{aligned} T^{\mathrm{kin}}_{(s_1,s_2,s_3)}(\mathbf{k}) = &-\hat{u}^{s_1}(\mathbf{k})\overline{\mathscr{F}[\nabla\cdot(u^{s_2}\mathbf{u}^{s_3})](\mathbf{k})} \\ &-\hat{v}^{s_1}(\mathbf{k})\overline{\mathscr{F}[\nabla\cdot(v^{s_2}\mathbf{u})^{s_3}](\mathbf{k})} \\ &-\hat{w}^{s_1}(\mathbf{k})\overline{\mathscr{F}[\nabla\cdot(w^{s_2}\mathbf{u}^{s_3})](\mathbf{k})}, \end{aligned} \tag{A10}$$

where the superscripts indicate the projections in (A1).

c. Hypo- and hyperviscosity

The hyperviscosity and hyperdiffusion terms of the form

$$-(-\nu_h^{1/d}\Delta_h^2 - \nu_z^{1/d}\partial_z^2)^d\mathbf{u} \quad \text{and} \quad -\frac{b}{N}(-\nu_h^{1/d}\Delta_h^2 - \nu_z^{1/d}\partial_z^2)^d\rho' \tag{A11}$$

have been applied to (1a) and (1b), respectively, to maintain stability and to provide a sink of energy within a localized dissipation range at small scales. Here the order of the hyperviscosity is $d = 8$. The hyperviscosity coefficients are computed based on resolution as

$$\begin{aligned} \nu_h &= \frac{1}{\tau k_{h,\max}^{2d}} = 6.34\times10^{-5}\,\mathrm{m}^{16}\,\mathrm{s}^{-1} \quad \text{and} \\ \nu_z &= \frac{1}{\tau k_{z,\max}^{2d}} = 4.16\times10^{-16}\,\mathrm{m}^{16}\,\mathrm{s}^{-1}. \end{aligned} \tag{A12}$$

where $k_{h,\max} = 84(2\pi/500\,\mathrm{m})$ and $k_{z,\max} = 42(2\pi/500\,\mathrm{m})$ are the maximum horizontal and vertical wavenumbers used after dealising.

On the other hand, a hypoviscosity is also applied, arresting the inverse transfer of energy to the largest scales and thereby allowing the system to reach a statistically steady state at long times (e.g., Danilov and Gurarie 2004). The hypoviscosity and hypodiffusion terms of the form

$$\begin{aligned} &-(-\nu_{h,2}^{-1/d_2}\Delta_h^2 - \nu_{z,2}^{-1/d_2}\partial_z^2)^{-d_2}\mathbf{u} \quad \text{and} \\ &-\frac{b}{N}(-\nu_{h,2}^{-1/d_2}\Delta_h^2 - \nu_{z,2}^{-1/d_2}\partial_z^2)^{-d_2}\rho' \end{aligned} \tag{A13}$$

are also applied to (1a) and (1b) with $d_2 = 4$. Similarly to the hyperviscosity case, the hypoviscosity are computed based on resolution as

$$\begin{aligned} \nu_{h,2} &= \frac{10k_{h,\min}^{d_2}}{\tau} = 9.37\times10^{-19}\,\mathrm{m}^{-8}\,\mathrm{s}^{-1} \quad \text{and} \\ \nu_{z,2} &= \frac{10k_{z,\min}^{d_2}}{\tau} = 9.37\times10^{-11}\,\mathrm{m}^{-8}\,\mathrm{s}^{-1}, \end{aligned} \tag{A14}$$

where $k_{h,\min} = 2\pi/500\,\mathrm{m}$ and $k_{z,\min} = 2\pi/50\,\mathrm{m}$ are the smallest horizontal and vertical wavenumbers.

The hyperviscosity (A11) and hypoviscosity (A13) are active in relatively narrow wavenumber bands at opposite ends of the energy spectrum, and thus maximize the range of simulation wavenumbers dominated by nonlinear effects in statistically steady state.

REFERENCES

Babin, A., A. Mahalov, B. Nicolaenko, and Y. Zhou, 1997: On the asymptotic regimes and the strongly stratified limit of rotating boussinesq equations. *Theor. Comput. Fluid Dyn.*, **9**, 223–251, https://doi.org/10.1007/s001620050042.

——, ——, and ——, 2000: Global regularity of 3D rotating Navier-Stokes equations for resonant domains. *Appl. Math. Lett.*, **13**, 51–57, https://doi.org/10.1016/S0893-9659(99)00208-6.

Balwada, D., J. H. LaCasce, K. G. Speer, and R. Ferrari, 2021: Relative dispersion in the Antarctic Circumpolar Current. *J. Phys. Oceanogr.*, **51**, 553–574, https://doi.org/10.1175/JPO-D-19-0243.1.

Barkan, R., K. Winters, and J. McWilliams, 2017: Stimulated imbalance and the enhancement of eddy kinetic energy dissipation by internal waves. *J. Phys. Oceanogr.*, **47**, 181–198, https://doi.org/10.1175/JPO-D-16-0117.1.

Bartello, P., 1995: Geostrophic adjustment and inverse cascades in rotating stratified turbulence. *J. Atmos. Sci.*, **52**, 4410–4428, https://doi.org/10.1175/1520-0469(1995)052<4410:GAAICI>2.0.CO;2.

Bennett, A. F., 1984: Relative dispersion: Local and nonlocal dynamics. *J. Atmos. Sci.*, **41**, 1881–1886, https://doi.org/10.1175/1520-0469(1984)041<1881:RDLAND>2.0.CO;2.

Beron-Vera, F., and J. LaCasce, 2016: Statistics of simulated and observed pair separations in the Gulf of Mexico. *J. Phys. Oceanogr.*, **46**, 2183–2199, https://doi.org/10.1175/JPO-D-15-0127.1.

Bodner, A. S., and B. Fox-Kemper, 2020: A breakdown in potential vorticity estimation delineates the submesoscale-to-turbulence boundary in large eddy simulations. *J. Adv. Model. Earth Syst.*, **12**, e2020MS002049, https://doi.org/10.1029/2020MS002049.

Boussinesq, J., 1877: Essai sur la théorie des eaux courantes. *C. R. Acad. Sci.*, **23**, 1–64.

Brunner-Suzuki, A.-M. E. G., M. Sundermeyer, and M.-P. Lelong, 2012: Vortex stability in a large-scale internal wave shear. *J. Phys. Oceanogr.*, **42**, 1668–1683, https://doi.org/10.1175/JPO-D-11-0137.1.

——, M. A. Sundermeyer, and M.-P. Lelong, 2014: Upscale energy transfer by the vortical mode and internal waves. *J. Phys. Oceanogr.*, **44**, 2446–2469, https://doi.org/10.1175/JPO-D-12-0149.1.

Bühler, O., N. Grisouard, and M. Holmes-Cerfon, 2013: Strong particle dispersion by weakly dissipative random internal waves. *J. Fluid Mech.*, **719**, R4, https://doi.org/10.1017/jfm.2013.71.

Charney, J. G., 1948: On the scale of atmospheric motions. *Geofys. Publ.*, **17** (2), 1–17.

——, 1971: Geostrophic turbulence. *J. Atmos. Sci.*, **28**, 1087–1095, https://doi.org/10.1175/1520-0469(1971)028<1087:GT>2.0.CO;2.

Danilov, S., and D. Gurarie, 2004: Scaling, spectra and zonal jets in beta-plane turbulence. *Phys. Fluids*, **16**, 2592–2603, https://doi.org/10.1063/1.1752928.

Early, J. J., M. P. Lelong, and M. A. Sundermeyer, 2021: A generalized wave-vortex decomposition for rotating Boussinesq flows with arbitrary stratification. *J. Fluid Mech.*, **912**, A32, https://doi.org/10.1017/jfm.2020.995.

Embid, P. F., and A. J. Majda, 1996: Averaging over fast gravity waves for geophysical flows with arbitrary potential vorticity. *Commun. Partial Differ. Equations*, **21**, 619–658, https://doi.org/10.1080/03605309608821200.

——, and ——, 1998: Low Froude number limiting dynamics for stably stratified flow with small or finite Rossby numbers.

Geophys. Astrophys. Fluid Dyn., **87**, 1–50, https://doi.org/10.1080/03091929808208993.

Essink, S., V. Hormann, L. Centurioni, and A. Mahadevan, 2019: Can we detect submesoscale motions in drifter pair dispersion. *J. Phys. Oceanogr.*, **49**, 2237–2254, https://doi.org/10.1175/JPO-D-18-0181.1.

Fitzgerald, J. G., and B. F. Farrell, 2018a: Statistical state dynamics of vertically sheared horizontal flows in two-dimensional stratified turbulence. *J. Fluid Mech.*, **854**, 544–590, https://doi.org/10.1017/jfm.2018.560.

——, and ——, 2018b: Vertically sheared horizontal flow-forming instability in stratified turbulence: Analytical linear stability analysis of statistical state dynamics equilibria. *J. Atmos. Sci.*, **75**, 4201–4227, https://doi.org/10.1175/JAS-D-18-0075.1.

Gamba, I., L. Smith, and M.-B. Tran, 2020: On the wave turbulence theory for stratified flows in the ocean. *Math. Models Methods Appl. Sci.*, **30**, 105–137, https://doi.org/10.1142/S0218202520500037.

Garrett, C. J. R., and W. Munk, 1979: Internal waves in the ocean. *Annu. Rev. Fluid Mech.*, **11**, 339–369, https://doi.org/10.1146/annurev.fl.11.010179.002011.

Gill, A. E., 1982: *Atmosphere–Ocean Dynamics*. Academic Press, 680 pp.

Hernández-Dueñas, G., L. M. Smith, and S. N. Stechmann, 2014: Investigation of Boussinesq dynamics using intermediate models based on wave–vortical interactions. *J. Fluid Mech.*, **747**, 247–287, https://doi.org/10.1017/jfm.2014.138.

Holmes-Cerfon, M., O. Bühler, and R. Ferrari, 2011: Particle dispersion by random waves in the rotating Boussinesq system. *J. Fluid Mech.*, **670**, 150–175, https://doi.org/10.1017/S0022112010005240.

Kraichnan, R. H., 1967: Inertial ranges in two-dimensional turbulence. *Phys. Fluids*, **10**, 1417–1423, https://doi.org/10.1063/1.1762301.

——, 1973: Helical turbulence and absolute equilibrium. *J. Fluid Mech.*, **59**, 745–752, https://doi.org/10.1017/S0022112073001837.

LaCasce, J. H., 2008: Statistics from Lagrangian observations. *Prog. Oceanogr.*, **77**, 1–29, https://doi.org/10.1016/j.pocean.2008.02.002.

Laval, J., J. McWilliams, and B. Dubrulle, 2003: Forced stratified turbulence: Successive transitions with Reynolds number. *Phys. Rev. E*, **68**, 036308, https://doi.org/10.1103/PhysRevE.68.036308.

Ledwell, J. R., A. Watson, and C. Law, 1993: Evidence for mixing across the pycnocline from an open ocean tracer release experiment. *Nature*, **364**, 701–703, https://doi.org/10.1038/364701a0.

——, T. F. Duda, M. A. Sundermeyer, and H. E. Seim, 2004: Mixing in a coastal environment: 1. A view from dye dispersion. *J. Geophys. Res.*, **109**, C10013, https://doi.org/10.1029/2003JC002194.

Lelong, M.-P., 1989: Weakly nonlinear internal wave/vortical mode interactions in stably-stratified flows. Ph.D. thesis, University of Washington, 101 pp.

——, and J. J. Riley, 1991: Internal wave-vortical mode interactions in strongly stratified flows. *J. Fluid Mech.*, **232**, 1–19, https://doi.org/10.1017/S0022112091003609.

——, and T. J. Dunkerton, 1998: Inertia-gravity wave breaking in three dimensions. Part I: Convectively stable waves. *J. Atmos. Sci.*, **55**, 2473–2488, https://doi.org/10.1175/1520-0469(1998)055<2473:IGWBIT>2.0.CO;2.

——, and M. A. Sundermeyer, 2005: Geostrophic adjustment of an isolated diapycnal mixing event and its implications for small-scale lateral dispersion. *J. Phys. Oceanogr.*, **35**, 2352–2367, https://doi.org/10.1175/JPO2835.1.

Lien, R.-C., and T. Sanford, 2019: Small-scale potential vorticity in the upper-ocean thermocline. *J. Phys. Oceanogr.*, **49**, 1845–1872, https://doi.org/10.1175/JPO-D-18-0052.1.

Lvov, Y. V., and E. G. Tabak, 2004: A Hamiltonian formulation for long internal waves. *Physica D*, **195**, 106–122, https://doi.org/10.1016/j.physd.2004.03.010.

——, K. L. Polzin, and E. G. Tabak, 2004: Energy spectra of the ocean's internal wave field: Theory and observations. *Phys. Rev. Lett.*, **92**, 128501, https://doi.org/10.1103/PhysRevLett.92.128501.

——, ——, ——, and N. Yokoyama, 2010: Oceanic internal-wave field: Theory of scale-invariant spectra. *J. Phys. Oceanogr.*, **40**, 2605–2623, https://doi.org/10.1175/2010JPO4132.1.

——, K. Polzin, and N. Yokoyama, 2012: Resonant and near-resonant internal wave interactions. *J. Phys. Oceanogr.*, **42**, 669–691, https://doi.org/10.1175/2011JPO4129.1.

Majda, A., 2003: *Introduction to PDEs and Waves for the Atmosphere and Ocean*. Courant Lecture Notes in Mathematics, Vol. 9, New York University Courant Institute of Mathematical Sciences, 234 pp.

McComas, C. H., and F. P. Bretherton, 1977: Resonant interaction of oceanic internal waves. *J. Geophys. Res.*, **82**, 1397–1412, https://doi.org/10.1029/JC082i009p01397.

McWilliams, J. C., 2008: Fluid dynamics at the margin of rotational control. *Environ. Fluid Mech.*, **8**, 441–449, https://doi.org/10.1007/s10652-008-9081-8.

Morel, Y., and J. C. McWilliams, 1997: Evolution of isolated interior vortices in the ocean. *J. Phys. Oceanogr.*, **27**, 727–748, https://doi.org/10.1175/1520-0485(1997)027<0727:EOIIVI>2.0.CO;2.

Müller, P., G. Holloway, F. Henyey, and N. Pomphrey, 1986: Nonlinear interactions among internal gravity waves. *Rev. Geophys.*, **24**, 493–536, https://doi.org/10.1029/RG024i003p00493.

Nazarenko, S., 2011: *Wave Turbulence*. Lecture Notes in Physics, Vol. 825, Springer, 279 pp., https://doi.org/10.1007/978-3-642-15942-8.

Newell, A. C., and B. Rumpf, 2011: Wave turbulence. *Annu. Rev. Fluid Mech.*, **43**, 59–78, https://doi.org/10.1146/annurev-fluid-122109-160807.

Pedlosky, J., 1982: *Geophysical Fluid Dynamics*. Vol. 1. Springer, 636 pp.

Polzin, K., and R. Ferrari, 2004: Isopycnal dispersion in NATRE. *J. Phys. Oceanogr.*, **34**, 247–257, https://doi.org/10.1175/1520-0485(2004)034<0247:IDIN>2.0.CO;2.

Remmel, M., 2010: New models for the rotating shallow water and Boussinesq equations by subsets of mode interactions. Ph.D. thesis, University of Wisconsin–Madison, 158 pp.

——, and L. Smith, 2009: New intermediate models for rotating shallow water and an investigation of the preference for anticyclones. *J. Fluid Mech.*, **635**, 321–359, https://doi.org/10.1017/S0022112009007897.

——, J. Sukhatme, and L. M. Smith, 2010: Nonlinear inertia-gravity wave-mode interactions in three dimensional rotating stratified flows. *Commun. Math. Sci.*, **8**, 357–376, https://doi.org/10.4310/CMS.2010.v8.n2.a4.

——, ——, and ——, 2014: Nonlinear gravity-wave interactions in stratified turbulence. *Theor. Comput. Fluid Dyn.*, **28**, 131–145, https://doi.org/10.1007/s00162-013-0305-2.

Rhines, P. B., 1988: Mixing and large-scale ocean dynamics. *Small-Scale Turbulence and Mixing in the Ocean*. J. Nihoul and B. Jamart, Eds., Elsevier Oceanography Series, Vol. 46, Elsevier, 263–284, https://doi.org/10.1016/S0422-9894(08)70552-X.

Rypina, I., J. Llopiz, L. Pratt, and M. Lozier, 2014: Dispersal pathways of American eel larvae from the Sargasso Sea. *Limnol. Oceanogr.*, **59**, 1704–1714, https://doi.org/10.4319/lo.2014.59.5.1704.

Salmon, R., 1983: Baroclinic instability and geostrophic turbulence. *Geophys. Astrophys. Fluid Dyn.*, **15**, 167–211, https://doi.org/10.1080/03091928008241178.

Shcherbina, A. Y., and Coauthors, 2015: The LatMix summer campaign: Submesoscale stirring in the upper ocean. *Bull. Amer. Meteor. Soc.*, **96**, 1257–1279, https://doi.org/10.1175/BAMS-D-14-00015.1.

Sinha, A., D. Balwada, N. Tarshish, and R. Abernathey, 2019: Modulation of lateral transport by submesoscale flows and inertia-gravity waves. *J. Adv. Model. Earth Syst.*, **11**, 1039–1065, https://doi.org/10.1029/2018MS001508.

Smith, L., and F. Waleffe, 2002: Generation of slow large scales in forced rotating stratified turbulence. *J. Fluid Mech.*, **451**, 145–168, https://doi.org/10.1017/S0022112001006309.

Sundermeyer, M. A., 1998: Studies of lateral dispersion in the ocean. Ph.D. thesis, Massachusetts Institute of Technology/Woods Hole Oceanographic Institution Joint Program, 215 pp., https://doi.org/10.1575/1912/8852.

——, and J. R. Ledwell, 2001: Lateral dispersion over the continental shelf: Analysis of dye-release experiments. *J. Geophys. Res.*, **106**, 9603–9621, https://doi.org/10.1029/2000JC900138.

——, and M.-P. Lelong, 2005: Numerical simulations of lateral dispersion by the relaxation of diapycnal mixing events. *J. Phys. Oceanogr.*, **35**, 2368–2386, https://doi.org/10.1175/JPO2834.1.

——, J. R. Ledwell, N. S. Oakey, and B. J. W. Greenan, 2005: Stirring by small-scale vortices caused by patchy mixing. *J. Phys. Oceanogr.*, **35**, 1245–1262, https://doi.org/10.1175/JPO2713.1.

——, M.-P. Lelong, E. L. Kunze, J. J. Early, and C. Wortham, 2020a: Pathways from internal-wave driven processes to vortical mode and submesoscale dispersion. *Ocean Sciences Meeting*, San Diego CA, Amer. Geophys. Union, Abstract PS41A-07, https://agu.confex.com/agu/osm20/meetingapp.cgi/Paper/654509.

——, D. Birch, J. R. Ledwell, M. D. Levine, S. D. Pierce, and B. T. K. Cervantes, 2020b: Dispersion in the open ocean seasonal pycnocline at scales of 1–10 km and 1–6 days. *J. Phys. Oceanogr.*, **50**, 415–437, https://doi.org/10.1175/JPO-D-19-0019.1.

Taylor, S., and D. Straub, 2016: Forced near-inertial motion and dissipation of low-frequency kinetic energy in a wind-driven channel flow. *J. Phys. Oceanogr.*, **46**, 79–93, https://doi.org/10.1175/JPO-D-15-0060.1.

Thomas, J., and D. Daniel, 2020: Turbulent exchanges between near-inertial waves and balanced flows. *J. Fluid Mech.*, **902**, A7, https://doi.org/10.1017/jfm.2020.510.

——, and ——, 2021: Forward flux and enhanced dissipation of geostrophic balanced energy. *J. Fluid Mech.*, **911**, A60, https://doi.org/10.1017/jfm.2020.1026.

Thomson, R., and W. Emery, 2014: *Data Analysis Methods in Physical Oceanography*. 3rd ed. Elsevier, 716 pp.

Torres, H. S., P. Klein, D. Menemenlis, B. Qiu, Z. Su, J. Wang, S. Chen, and L.-L. Fu, 2018: Partitioning ocean motions into balanced motions and internal gravity waves: A modeling study in anticipation of future space missions. *J. Geophys. Res. Oceans*, **123**, 8084–8105, https://doi.org/10.1029/2018JC014438.

Vallis, G. K., 2017: *Atmospheric and Oceanic Fluid Dynamics: Fundamentals and Large-Scale Circulation*. 2nd ed. Cambridge University Press, 946 pp., https://doi.org/10.1017/9781107588417.

Wagner, G. L., and W. R. Young, 2016: A three-component model for the coupled evolution of near-inertial waves, quasi-geostrophic flow and the near-inertial second harmonic. *J. Fluid Mech.*, **802**, 806–837, https://doi.org/10.1017/jfm.2016.487.

Waite, M. L., and P. Bartello, 2006: The transition from geostrophic to stratified turbulence. *J. Fluid Mech.*, **568**, 89–108, https://doi.org/10.1017/S0022112006002060.

Whalen, C. B., C. de Lavergne, A. C. Naveira Garabato, J. M. Klymak, J. A. MacKinnon, and K. L. Sheen, 2020: Internal wave-driven mixing: Governing processes and consequences for climate. *Nat. Rev. Earth Environ.*, **1**, 606–621, https://doi.org/10.1038/s43017-020-0097-z.

Xie, J.-H., and J. Vanneste, 2015: A generalized-lagrangian-mean model of the interactions between near-inertial waves and mean flow. *J. Fluid Mech.*, **774**, 143–169, https://doi.org/10.1017/jfm.2015.251.

Young, W. R., P. B. Rhines, and C. J. R. Garrett, 1982: Shear-flow dispersion, internal waves and horizontal mixing in the ocean. *J. Phys. Oceanogr.*, **12**, 515–527, https://doi.org/10.1175/1520-0485(1982)012<0515:SFDIWA>2.0.CO;2.

Zakharov, V. E., V. S. Lvov, and G. Falkovich, 1992: *Kolmogorov Spectra of Turbulence 1. Wave Turbulence*. Springer, 264 pp.